

Gaussian Process Landmarking on Manifolds

Tingran Gao ^{*} Shahar Z. Kovalsky [†] Doug M. Boyer [‡] Ingrid Daubechies [§]

June 7, 2021

Abstract

As a means of improving analysis of biological shapes, we propose a greedy algorithm for sampling a Riemannian manifold based on the uncertainty of a Gaussian process. This is known to produce a near optimal experimental design with the manifold as the domain, and appears to outperform the use of user-placed landmarks in representing geometry of biological objects. We provide an asymptotic analysis for the decay of the maximum conditional variance, which is frequently employed as a greedy criterion for similar variance- or uncertainty-based sequential experimental design strategies; to our knowledge this is the first result of this type for experimental design. The key observation is to link the greedy algorithm with reduced basis methods in the context of model reduction for partial differential equations. We apply the proposed landmarking algorithm to geometric morphometrics, a branch of evolutionary biology focusing on the analysis and comparisons of anatomical shapes, and compare the automatically sampled landmarks with the “ground truth” landmarks manually placed by evolutionary anthropologists; the results suggest that Gaussian process landmarks perform equally well or better, in terms of both spatial coverage and downstream statistical analysis. We expect this approach will find additional applications in other fields of research.

Keywords: Gaussian Process, Experimental Design, Active Learning, Manifold Learning, Reduced Basis Methods, Geometric Morphometrics, Procrustes Distance

1 Introduction

This paper applies principles of the statistics field of *optimal experimental design* to *geometric morphometrics*. In contrast to methods for statistical estimation and inference, which typically focus on studying the error made by estimators with respect to a finite collection of sample observations (generated either randomly or deterministically) and selecting the estimator so as to minimize this error, given a (fixed) collection of samples, the paradigm of optimal experimental design is to minimize the empirical risk by an “optimal” choice of sample locations, while the estimator itself and the number of samples are kept fixed [110, 6]. Finding an optimal design amounts to choosing sample points that are most informative for a class of estimators so as to reduce the number of observations; this is most desirable when even one observation is expensive to acquire (e.g. in spatial analysis (geostatistics) [137, 33] and computationally demanding computer experiments [122]), but similar ideas have long been exploited in the probabilistic analysis of more classical numerical analysis problems (see e.g. [133, 150, 114]).

Geometric morphometrics is a subfield of evolutionary biology that focuses on quantifying the (dis-)similarities between pairs of two-dimensional anatomical surfaces based on their spatial configurations. These analyses typically start with manually identifying an equal number of geometrically or semantically meaningful feature points, or *landmarks*, on each specimen in a potentially large collection of anatomical surfaces; the landmarks are certified by domain experts to be in consistent one-to-one correspondences. Pairwise or group-wise Procrustes analysis [54, 38, 55] is then applied to quantitatively compare the specimens in the collection; these quantitative comparison results are then subject to further statistical analysis to draw biologically relevant conclusions for the dataset.

In this paper, we adopt the methodology of optimal experimental design for discretely sampling Riemannian manifolds, and illustrate the effectiveness of our approach on anatomical surfaces stemming from evolutionary anthropology. We consider this application as prototypical; i.e. we expect that the approach we propose here can be

^{*}Department of Statistics, The University of Chicago, Chicago, IL 60637, USA (tingrango@galton.uchicago.edu).

[†]Department of Mathematics, Duke University, Durham, NC 27708, USA (shaharko@math.duke.edu).

[‡]Department of Evolutionary Anthropology, Duke University, Durham NC 27708, USA (doug.boyer@duke.edu).

[§]Department of Mathematics and Department of Electrical and Computer Engineering, Duke University, Durham NC 27708, USA (ingrid@math.duke.edu).

applied more widely, to other application domains. In contexts different from evolutionary biology, closely related (continuous or discretized) manifold sampling problems are addressed in [5, 87, 59], where smooth manifolds are discretized by optimizing the locations of (a fixed number of) points so as to minimize a Riesz functional, or by [102], studying surface simplification via spectral subsampling. These approaches, however, tend to distribute points uniformly when applied to two-dimensional surfaces, whereas our motivation is rooted in the application of geometric morphometrics, for which informative geometric features needed for effective downstream statistical shape analysis are typically neither uniformly distributed nor naturally associated with an energy potential. Instead, our work is inspired by recent research on active learning with Gaussian processes [31, 113, 66] as well as related applications in finding landmarks along a manifold [75]. Our approach considers a Gaussian process on the manifold whose covariance structure is specified by the heat kernel. In turn, we design a greedy landmarking strategy which aims to produce a set of geometrically-significant samples.

The main objects of study in geometric morphometrics are anatomical surfaces of extinct and extant animals; we will focus on the surfaces of bones and teeth of particular interest for evolutionary biologists. With the advancement of digitization technologies, discrete triangular mesh representations of continuous biological surfaces are readily available and are used for high throughput analysis for large collections of specimens. We will thus focus on two-dimensional surfaces represented by discrete triangular meshes. We denote a triangular mesh with notation $G = (V, E, F)$, where V , E , F stand for the set of vertices, edges, and faces, respectively. To see the link between landmark identification and active learning with uncertainty sampling [74, 126], let us consider the regression problem of estimating a function $f : V \rightarrow \mathbb{R}$ defined over the vertices of a triangular mesh G . However, rather than construct the estimator from random sample observations, we adopt the point of view of active learning, in which one is allowed to sequentially query the values of f at user-picked vertices $x \in V$. In order to minimize the empirical risk of an estimator \hat{f} within a given number of iterations, the simplest and most commonly used strategy is to first evaluate (under reasonable probabilistic model assumptions) the informativeness of the vertices on the mesh that have not been queried, and then greedily choose to inquire the value of f at the vertex x at which the response value $\hat{f}(x)$ —inferred from all previous queries—is most “uncertain” in the sense of attaining highest conditional variance (other uncertainty measures could be used as well, such as the Shannon entropy); these sequentially obtained points of highest uncertainties will be treated as morphometrical *landmarks* in our proposed algorithm.

This straightforward application of an active learning strategy relies upon selecting a regression function f of rich biological information. In the absence of a natural candidate regression function f , we seek to reduce in every iteration the maximum “average uncertainty” of a class of regression functions, e.g., specified by a Gaussian process prior [113]. Throughout this paper we will denote $\text{GP}(m, K)$ for the Gaussian process on a smooth, compact Riemannian manifold M with mean function $m : M \rightarrow \mathbb{R}$ and covariance function $K : M \times M \rightarrow \mathbb{R}$. If we interpret choosing a single most “biologically meaningful” function f as a manual “feature handcrafting” step, the specification of a Gaussian process prior can be viewed as a less restrictive and more stable “ensemble” version; the geometric information can be conveniently encoded into the prior by specifying an appropriate covariance function K . We construct such a covariance function in Section 3 by reweighting the heat kernel of the Riemannian manifold M , adopting (but in the meanwhile also appending further geometric information to) the methodology of Gaussian process optimal experimental design [120, 122, 39] and *sensitivity analysis* [121, 101] from the statistics literature.

Our Contributions. The main contribution in this paper is three-fold: First, we propose to automatically landmark an anatomical surface using a greedy procedure in Gaussian process active learning, and demonstrate the efficacy and informativeness of the resulting landmarks in analyzing real datasets in geometric morphometrics. Second, our approach utilizes a Gaussian process defined by a reweighted heat kernel, which has not been studied in the existing manifold learning literature; nonetheless, we show that, in the continuous limit, the reweighted kernel converges pointwise to a Fokker-Planck operator determined by the weight function, akin to a properly reweighted kernel in diffusion maps. Third, we provide a convergence rate analysis for the greedy algorithm of uncertainty-based sequential experimental design, which amounts to estimating the uniform rate of decay for the conditional variance of a Gaussian process as the number of greedily picked design points approaches infinity; on a C^∞ -manifold we deduce that the convergence is faster than any inverse polynomial rate, which is the optimal rate any non-greedy landmarking algorithm can attain on a generic smooth manifold. This analysis makes use of recent results in the analysis of reduced based methods. To our knowledge, this is the first analysis of this type for greedy algorithms in optimal experimental design; the convergence results obtained from this analysis can also be used to bound the number of iterations in Gaussian process active learning [31, 66, 75] and maximum entropy design [122, 73, 100].

The rest of this paper is organized as follows. Section 2 sets notations and provides background materials for Gaus-

sian processes and geometric morphometrics; Section 3 details the construction of heat kernels on triangular meshes, as well as the “reweighted kernel” constructed from these discretized heat kernels; Section 4 presents the unsupervised landmarking algorithm for anatomical surfaces inspired by recent work on uncertainty sampling in Gaussian process active learning [75]; Section 5 provides deeper theoretical insights for the mechanism of the landmarking algorithm by connecting it with manifold learning, maximum entropy experimental design, and reduced based method; Section 6 demonstrates several applications of the proposed algorithm in automated geometric morphometrics; Section 7 summarizes the current paper with a discussion and a brief sketch of potential future directions.

2 Background

This section introduces the notations that will be used throughout this paper. We describe Gaussian processes on a Riemannian manifold with the heat kernel as covariance functions, and provide background information for the geometric morphometrics application that motivated this paper.

2.1 Heat Kernels and Gaussian Processes on Riemannian Manifolds: A Spectral Embedding Perspective

Let (M, g) be an orientable compact Riemannian manifold of dimension $d \geq 1$ with finite volume, where g is the Riemannian metric on M . Denote $d\text{vol}_M$ for the canonical volume form M with coordinate representation

$$d\text{vol}_M(x) = \sqrt{|g(x)|} dx^1 \wedge \cdots \wedge dx^d.$$

The finite volume will be denoted as

$$\text{Vol}(M) = \int_M d\text{vol}_M(x) = \int_M \sqrt{|g(x)|} dx^1 \wedge \cdots \wedge dx^d < \infty,$$

and we will fix the canonical normalized volume form $d\text{vol}_M/\text{Vol}(M)$ as reference. Throughout this paper, all distributions on M are absolutely continuous with respect to $d\text{vol}_M/\text{Vol}(M)$.

The single-output regression problem on the Riemannian manifold M will be described as follows. Given independent and identically distributed observations $\{(X_i, Y_i) \in M \times \mathbb{R} \mid 1 \leq i \leq n\}$ of a random variable (X, Y) on the product probability space $M \times \mathbb{R}$, the goal of the regression problem is to estimate the conditional expectation

$$f(x) := \mathbb{E}(Y \mid X = x) \tag{1}$$

which is often referred to as a regression function of Y on X [140]. The joint distribution of X and Y will always be assumed absolutely continuous with respect to the product measure on $M \times \mathbb{R}$ for simplicity. A Gaussian process (or *Gaussian random field*) on M with mean function $m : M \rightarrow \mathbb{R}$ and covariance function $K : M \times M \rightarrow \mathbb{R}$ is defined as the stochastic process of which any finite marginal distribution on n fixed points $x_1, \dots, x_n \in M$ is a multivariate Gaussian distribution with mean vector

$$m(\{x_1, \dots, x_n\}) := (m(x_1), \dots, m(x_n)) \in \mathbb{R}^n$$

and covariance matrix

$$K(\{x_1, \dots, x_n\}) := \begin{pmatrix} K(x_1, x_1) & \cdots & K(x_1, x_n) \\ \vdots & & \vdots \\ K(x_n, x_1) & \cdots & K(x_n, x_n) \end{pmatrix} \in \mathbb{R}^{n \times n}.$$

A Gaussian process with mean function $m : M \rightarrow \mathbb{R}$ and covariance function $K : M \times M \rightarrow \mathbb{R}$ will be denoted as $\text{GP}(m, K)$, as stated in Section 1.

We will frequently make use of the Reproducing Kernel Hilbert Space (RKHS) framework (see e.g. [34, 92]) \mathcal{H}_K on M with kernel function K . For any positive semi-definite symmetric kernel function $K : M \times M \rightarrow \mathbb{R}$, Mercer’s Theorem [34, Theorem 3.6] states that K admits a uniformly convergent expansion of the form

$$K(x, y) = \sum_{i=0}^{\infty} e^{-\lambda_i} \phi_i(x) \phi_i(y), \quad \forall x, y \in M,$$

where $\{\phi_i\}_{i=0}^\infty \subset L^2(M)$ are the eigenfunctions of the integral operator $T_K : L^2(M) \rightarrow L^2(M)$ defined by

$$T_K f(x) := \int_M K(x, y) f(y) \, d\text{vol}_M(y), \quad \forall f \in L^2(M)$$

and $e^{-\lambda_i}, i = 0, 1, \dots$, ordered so that $e^{-\lambda_0} \geq e^{-\lambda_1} \geq e^{-\lambda_2} \geq \dots$, are the eigenvalues of this integral operator corresponding to the eigenfunctions $\phi_i, i = 0, 1, \dots$, respectively. Regression under this framework amounts to restricting the regression function to lie in the Hilbert space

$$\mathcal{H}_K := \left\{ f = \sum_{i=0}^\infty \alpha_i \phi_i \mid \alpha_i \in \mathbb{R}, \sum_{i=0}^\infty e^{\lambda_i} \alpha_i^2 < \infty \right\} \quad (2)$$

on which the inner product is defined as

$$\langle f, g \rangle_{\mathcal{H}_K} = \sum_{i=0}^\infty e^{\lambda_i} \langle f, \phi_i \rangle_{L^2(M)} \langle g, \phi_i \rangle_{L^2(M)}. \quad (3)$$

The reproducing property is reflected in the identity

$$\langle K(\cdot, x), K(\cdot, y) \rangle_{\mathcal{H}_K} = K(x, y) \quad \forall x, y \in M. \quad (4)$$

Borrowing terminologies from kernel-based learning methods (see e.g. [34] and [123]), the eigenfunctions and eigenvalues of T_K define a *feature mapping*

$$M \ni x \mapsto \Phi(x) := (e^{-\lambda_0/2} \phi_0(x), e^{-\lambda_1/2} \phi_1(x), \dots, e^{-\lambda_i/2} \phi_i(x), \dots) \in \ell^2$$

such that the kernel value $K(x, y)$ at an arbitrary pair $x, y \in M$ is given exactly by the inner product of $\Phi(x)$ and $\Phi(y)$ in the feature space ℓ^2 , i.e.

$$K(x, y) = \langle \Phi(x), \Phi(y) \rangle_{\ell^2}, \quad \forall x, y \in M,$$

and we have

$$\mathcal{H}_K = \left\{ f = \sum_{i=0}^\infty \beta_i \cdot e^{-\lambda_i/2} \phi_i = \langle \beta, \Phi \rangle_{\ell^2} \mid \beta = (\beta_0, \beta_1, \dots, \beta_i, \dots) \in \ell^2 \right\}.$$

In words, the RKHS framework embeds the Riemannian manifold M into an infinite dimensional Hilbert space ℓ^2 , and converts the (generically) nonlinear regression problem on M into a linear regression problem on a subset of ℓ^2 .

On Riemannian manifolds, there is a natural choice for the kernel function: the heat kernel of the Laplace-Beltrami operator. Denote $\Delta : C^2(M) \rightarrow C^2(M)$ for the Laplace-Beltrami operator on M with respect to the metric g , i.e.

$$\Delta f = \frac{1}{\sqrt{|g|}} \partial_i \left(\sqrt{|g|} g^{ij} \partial_j f \right), \quad \forall f \in C^\infty(M)$$

where the sign convention is such that $-\Delta$ is positive semidefinite. If the manifold M has no boundary, the spectrum of $-\Delta$ is well-known to be real, non-negative, discrete, with eigenvalues satisfying $0 = \lambda_0 < \lambda_1 \leq \lambda_2 \leq \dots \nearrow \infty$, with ∞ the only accumulation point of the spectrum; when M has non-empty boundary we assume Dirichlet boundary condition so the same conclusion holds for the eigenvalues. If we denote ϕ_i for the eigenfunction of Δ corresponding to the eigenvalue λ_i , then the set $\{\phi_i \mid i = 0, 1, \dots\}$ constitutes an orthonormal basis for $L^2(M)$ under the standard inner product

$$\langle f_1, f_2 \rangle_M := \int_M f_1(x) f_2(x) \, d\text{vol}_M(x).$$

The heat kernel $k_t(x, y) := k(x, y; t) \in C^2(M \times M) \times C^\infty((0, \infty))$ is the fundamental solution of the heat equation on M :

$$\partial_t u(x, t) = -\Delta u(x, t), \quad x \in M, t \in (0, \infty).$$

That is, if the initial data is specified as

$$u(x, t = 0) = v(x)$$

then

$$u(x, t) = \int_M k_t(x, y) v(y) \, d\text{vol}_M(y).$$

In terms of the spectral data of Δ as (see e.g. [116, 13]), the heat kernel can be written as

$$k_t(x, y) = \sum_{i=0}^{\infty} e^{-\lambda_i t} \phi_i(x) \phi_i(y), \quad \forall t \geq 0, \quad x, y \in M. \quad (5)$$

For any fixed $t > 0$, the heat kernel defines a Mercer kernel on M by

$$(x, y) \mapsto k_t(x, y) \quad \forall (x, y) \in M \times M$$

and the feature mapping takes the form

$$M \ni x \mapsto \Phi_t(x) := (e^{-\lambda_0 t/2} \phi_0(x), e^{-\lambda_1 t/2} \phi_1(x), \dots, e^{-\lambda_i t/2} \phi_i(x), \dots) \in \ell^2. \quad (6)$$

Note in particular that

$$k_t(x, y) = \langle \Phi_t(x), \Phi_t(y) \rangle_{\ell^2}. \quad (7)$$

In fact, up to a multiplicative constant $c(t) = \sqrt{2} (4\pi)^{\frac{d}{4}} t^{\frac{n+2}{4}}$, the feature mapping $\Phi_t : M \rightarrow \ell^2$ has long been studied in spectral geometry [12] and is known to be an embedding of M into ℓ^2 ; furthermore, with the multiplicative correction by $c(t)$, the pullback of the canonical metric on ℓ^2 is asymptotically equal to the Riemannian metric on M .

In this paper we focus on Gaussian processes on Riemannian manifolds with heat kernels (or “reweighted” counterparts thereof; see Section 3.2) as covariance functions. There are at least two reasons for heat kernels to be considered as natural candidates for covariance functions of Gaussian processes on manifolds. On the one hand, as argued in [25, §2.5], the abundant geometric information encoded in the Laplace-Beltrami operator makes the heat kernel a canonical choice for Gaussian processes; Gaussian processes defined this way impose natural geometric priors based on randomly rescaled solutions of the heat equation. On the other hand, by (7), a Gaussian process on M with heat kernel is equivalent to a Gaussian process on the embedded image of M into ℓ^2 under the feature mapping (6) with a dot product kernel; this is reminiscent of the methodology of *extrinsic Gaussian process regression* (eGPR) [76] on manifolds — in order to perform Gaussian process regression on a nonlinear manifold, eGPR first embeds the manifold into a Euclidean space using an arbitrary embedding, then perform Gaussian process regression on the embedded image following standard procedures for Gaussian process regression. This spectral embedding interpretation also underlies recent work constructing Gaussian priors, by means of the graph Laplacian, for uncertainty quantification of graph semi-supervised learning [15].

2.2 Geometric Morphometrics: Old and New

Statistical shape analysis, often termed *geometric morphometrics* in comparative biology, is the quantitative analysis of variations and correlations among biological forms through the Cartesian coordinates of “landmarks”—biologically informative, repeatable, and in some sense corresponding anatomical loci—on surfaces representing anatomy of biological organisms [151, 1]. In order for the comparisons across specimens to be meaningful, practitioners in this field often require that the landmarks be consistently annotated on each specimen in a manner reflecting the “operational homology”¹ or “biological correspondence” (as discussed in [20]) across individuated traits inherited from a common ancestry [89]. For instance, in the *generalized Procrustes analysis* (GPA) framework [54, 38, 55, 2], the *Procrustes distance* between two surfaces S_1, S_2 is computed using the following procedure:

- Specify two sets of operationally homologous landmarks $\{x_\ell^{(1)} \mid 1 \leq \ell \leq L\}, \{x_\ell^{(2)} \mid 1 \leq \ell \leq L\}$ on S_1, S_2 , respectively;
- Compute the distance between S_1 and S_2 by minimizing the energy functional

$$d_{\text{CP}}(S_1, S_2) = \inf_{T \in \mathbb{E}(3)} \left(\frac{1}{L} \sum_{\ell=1}^L \|T(x_\ell^{(1)}) - x_\ell^{(2)}\|^2 \right)^{\frac{1}{2}} \quad (8)$$

where $\mathbb{E}(3)$ is the group of rigid motions in \mathbb{R}^3 .

¹The term “homology” in the context of evolutionary theory bears a different meaning than in modern topology; see e.g. [115, Part IV].

This idea can be generalized to analyze a collection of consistently landmarked shapes, either assuming each set of landmarks on the same shape is centered at the origin so the variational problem is defined on a product space of orthogonal groups [55, 98, 136, 95], or estimate the optimal orthogonal and translation group elements jointly without the overall centering assumption [26].

The key to successfully applying the Procrustes framework in statistical shape analysis is to obtain an equal number of consistent, operationally homologous landmarks on every shape in a potentially enormous collection of shapes. Consistently landmarking a collection of shapes relies crucially upon domain knowledge and tedious manual labor, and the skill to perform it “correctly” typically requires years of professional training; even then the “correctness” can be subject to debate among experts (see e.g. [19] for an example on *Lepilemur* teeth). In the first place, extracting a finite number of landmarks from a continuous surface inevitably loses geometric information, unless when the shapes under consideration are easily seen to be uniquely determined by the landmarks (e.g. planar polygonal shapes, as considered in [68][40]), which is rarely the case for geometric morphometricians in biology; this problem of “inadequate coverage” motivated the introduction of *semilandmarks*—additional points along curves containing critical curvature information about the morphology—to compensate for the loss of geometry in the landmarking process. Unfortunately, the essential arbitrariness of the semilandmarks along a curve induces additional uncertainty that needs to be quantified and reduced [151, §2], especially in the absence of sharp anatomical features; the constraint of picking an equal number of landmarks on each shape also turns out to be far too artificial when the anatomical forms undergo complex evolutionary and developmental processes.

To mitigate both the scalability and the subjectivity issues in the existing Procrustes analysis framework, a recent trend of research in geometric morphometrics advocates *automated* workflows to bypass the repetitive, laborious, and time-consuming process of manual landmark placement; see e.g. [2, 19, 109, 79, 18, 80, 20, 42, 143, 70, 62] and the references therein. This type of technique works directly with digitized anatomical surfaces encoded in the data structure of discrete triangular meshes; numerical algorithms are combined with computer graphics and geometry processing to provide high throughput, landmark-free approaches for precise phenotyping [107, 60, 61] on the discrete triangular meshes on their entirety (often consisting of thousands to millions of vertices in \mathbb{R}^3), without the manual landmarking stage to filter down the number of variables using *a priori* domain knowledge. As much as the proponents of landmark-based morphometrics claim that landmark coordinates contain the information utilized in more traditional, measurement-based morphometrics as a proper subset [151, §2], the precursors of automated geometric morphometrics believe that using whole surfaces as input to their analysis passes even more information to the downstream analysis than the few dozens of landmarks.

Despite the capability of generating high quality pairwise shape registrations, the automated geometric morphometric methods suffer from interpretability problems: since all comparisons are performed merely pairwise, composing the obtained correspondences along a closed loop does not give rise to an identity map in general. This lack of *transitivity* (see e.g. [45, 43]) demands additional post-processing steps to translate the pairwise results into familiar input data to standard downstream phylogenetic analysis [103, 46], which bears a strong similarity with recent studies in synchronization problems [26, 44]. The loop inconsistency of pairwise correspondences also challenges the interpretability of automated geometric morphometrics, since it becomes virtually impossible to identify functionally equivalent regions across distinct anatomical structures in a consistent manner. Until fully automated geometric morphometric algorithms reach the maturity with comparable explanatory power to a human practitioner of landmark-based geometric morphometrics, deeper and more systematic understanding of the landmarking process still seem of great interest and value.

The methodology we propose in this paper incorporates an algorithmic landmarking procedure into the automated pairwise registration algorithms. As will be detailed in Section 6, we will first generate a set of candidate landmarks on each of the anatomical surfaces based on the “uncertainty” modeled by a Gaussian process, then apply a matching scheme that filters out non-corresponding candidate landmarks between a pair of surfaces based upon bounded conformal distortion [78]. Detecting morphometrically meaningful landmarks on anatomical surfaces in a completely unsupervised manner is a daunting task, since some of the most reliable landmarks are determined by patterns of juxtapositions of tissues—termed “Type 1 landmarks” by Bookstein [117]—which is almost always absent on the triangular meshes input to automated algorithms [17]. The selection process is further complicated by the requirement of the consistency of relative landmark positions across the data collected, as well as the specific functionality of the biological organism being studied [151]. While geometry processing algorithms (e.g. [8, 82, 24, 22, 139]) are capable of detecting sharp geometric features dictated by metric or topology (Bookstein’s “Type 2 landmarks” [117]), as well as producing high quality pairwise registrations for accurate determination of operationally homologous loci, semilandmarks and a majority of “Type 3 landmarks” in Bookstein’s typology of landmarks are marked simply for

adequate and/or comprehensive coverage of the anatomical forms [117]. For instance, some Type 3 landmarks are included in the analysis for being “furthest away” from sharp geometric or functional features [151]. These observations motivated us to consider algorithmic analogies of geometric morphologists’ daily practice beyond the scope of computational geometry, shedding light upon landmark identification from the perspective of Bayesian statistics quantifying the “uncertainty” of morphometric analysis.

3 Reweighted Heat Kernels

3.1 Discrete Heat Kernels on Point Clouds

When the Riemannian manifold M is a submanifold embedded in an ambient Euclidean space \mathbb{R}^D ($D \gg d$) and sampled only at finitely many number of points $\{x_1, \dots, x_n\}$, we know from the literature of Laplacian eigenmaps [10, 11] and diffusion maps [32, 130, 131] that the extrinsic squared exponential kernel matrix

$$K = (K_{ij})_{1 \leq i, j \leq n} = \left(\exp \left(-\frac{\|x_i - x_j\|^2}{t} \right) \right)_{1 \leq i, j \leq n} \quad (9)$$

is a consistent estimator (up to a multiplicative constant) of the heat kernel of the manifold M if $\{x_i \mid 1 \leq i \leq n\}$ are sampled uniformly and i.i.d. on M with appropriately adjusted bandwidth parameter $t > 0$ as $n \rightarrow \infty$; similar results holds when the squared exponential kernel is replaced with any anisotropic kernel, and additional renormalization techniques can be used to adjust the kernel if the samples are i.i.d. but not uniformly distributed on M , see e.g. [32] for more details. These theoretical results in manifold learning justifies using extrinsic kernel functions in a Gaussian process regression framework when the manifold is an embedded submanifold of an ambient Euclidean space; the kernel (9) is also used in [148] for Gaussian process regression on manifolds in a Bayesian setting.

3.2 Reweighted Kernels

The heat kernel of the Riemannian manifold M defines covariance functions for a family of Gaussian processes on M , but this type of covariance functions only depend on the spectral properties of M , whereas in practice we would often like to incorporate prior information addressing relative high/low confidence of the selected landmarks. For example, the response variables might be measured with higher accuracy (or equivalently the influence of random observation noise is damped) where the predictor falls on a region on the manifold M with lower curvature. We encode this type of prior information regarding the relative importance of different locations on the domain manifold in a smooth positive weight function $w : M \rightarrow \mathbb{R}_+$ defined on the entire manifold, of which the higher values of $w(x)$ indicates a relatively higher importance if a predictor variable is sampled near $x \in M$. Since we assume M is closed, w is bounded below away from zero. To “knit” the weight function into the heat kernel, notice that by the reproducing property we have

$$k_t(x, y) = \int_M k_{t/2}(x, z) k_{t/2}(z, y) \, \text{dvol}_M(z) \quad (10)$$

and we can naturally apply the weight function to deform the volume form, i.e. define

$$k_t^w(x, y) = \int_M k_{t/2}(x, z) k_{t/2}(z, y) w(z) \, \text{dvol}_M(z). \quad (11)$$

Obviously, $k_t^w(\cdot, \cdot) = k_t(\cdot, \cdot)$ on $M \times M$ if we pick $w \equiv 1$ on M , using the expression (5) for heat kernel $k_t(\cdot, \cdot)$ and the orthonormality of the eigenfunctions $\{\phi_i \mid i = 0, 1, \dots\}$. Intuitively, (11) reweights the mutual interaction between different regions on M such that the portions with high weights have a more significant influence on the covariance structure of the Gaussian process on M . The rest of the analysis for spectral Gaussian process in Section 3.1 carry through after replacing $\text{GP}(m, k_t)$ with $\text{GP}(m, k_t^w)$.

In practice, when the manifold is sampled only at finitely many i.i.d. points $\{x_1, \dots, x_n\}$ on M , the reweighted kernel can be calculated from the discrete extrinsic kernel matrix in (9) as

$$K^w = (K_{ij}^w)_{1 \leq i, j \leq n} = \left(\sum_{k=1}^n \exp \left(-\frac{\|x_i - x_k\|^2}{t/2} \right) \cdot w(x_k) \cdot \exp \left(-\frac{\|x_k - x_j\|^2}{t/2} \right) \right)_{1 \leq i, j \leq n} = K^\top W K \quad (12)$$

where W is a diagonal matrix of size $n \times n$ with $w(x_k)$ at its k -th diagonal entry, for all $1 \leq k \leq n$, and K is the discrete squared exponential kernel matrix in (9). It is worth point out that the reweighted kernel K^w no longer equals the kernel K in (9) when we set $w \equiv 1$ at this discrete level. The form of the reweighted kernel (11) has also appeared in [27] as the symmetrization of an asymmetric anisotropic kernel.

Though the reweighting step appears to be a straightforward implementation trick, it turns out to be crucial in the application of automated geometric morphometrics—the landmarking algorithm that will be presented in Section 4 produces biologically much more representative features on anatomical surfaces when the reweighted kernel is adopted. We shall illustrate this in greater detail in Section 6.

4 Gaussian Process Landmarking as Sequential Experimental Design

We present in this section an algorithm motivated by [75] that automatically places “landmarks” on a compact Riemannian manifold using a Gaussian process active learning strategy. Let us begin with an arbitrary nonparametric regression model in the form of (1). Unlike in standard supervised learning in which a finite number of sample-label pairs are provided, an active learning algorithm can iteratively decide, based on memory of all previously inquired sample-label pairs, which sample to inquire for label in the next step. In other words, given sample-label pairs $(X_1, Y_1), (X_2, Y_2), \dots, (X_{n-1}, Y_{n-1})$ observed up to the n -th step, an active learning algorithm can decide which sample X_n to query for the label information $Y_n = f(X_n)$ of the regression function f to be estimated; typically, the algorithm assumes full knowledge of the sample domain, has access to the regression function f as a black box, and strives to optimize its query strategy so as to estimate f in as few steps as possible. With a Gaussian process prior $\text{GP}(m, K)$ on the regression function class, the joint distribution of a finite collection of response values (Y_1, \dots, Y_n) is assumed to follow a multivariate Gaussian distribution $\mathcal{N}(m(X_1, \dots, X_n), K(X_1, \dots, X_n))$ where

$$m(X_1, \dots, X_n) = \begin{pmatrix} m(X_1) \\ \vdots \\ m(X_n) \end{pmatrix} \in \mathbb{R}^n, \quad K(X_1, \dots, X_n) = \begin{pmatrix} K(X_1, X_1) & \dots & K(X_1, X_n) \\ \vdots & & \vdots \\ K(X_n, X_1) & \dots & K(X_n, X_n) \end{pmatrix} \in \mathbb{R}^{n \times n}. \quad (13)$$

For simplicity of statement, introduce the following short-hand notations:

$$X_{n-1}^1 = \begin{pmatrix} X_1 \\ \vdots \\ X_{n-1} \end{pmatrix}, \quad Y_{n-1}^1 = \begin{pmatrix} Y_1 \\ \vdots \\ Y_{n-1} \end{pmatrix}, \quad K(X, X_{n-1}^1) = \begin{pmatrix} K(X, X_1) \\ \vdots \\ K(X, X_{n-1}) \end{pmatrix}, \quad K_{n-1} = \begin{pmatrix} K(X_1, X_1) & \dots & K(X_1, X_{n-1}) \\ \vdots & & \vdots \\ K(X_{n-1}, X_1) & \dots & K(X_{n-1}, X_{n-1}) \end{pmatrix}.$$

Given $(n-1)$ observed samples $(X_1, Y_1), \dots, (X_{n-1}, Y_{n-1})$, at any $X \in M$, the conditional probability of the response value $Y(X) | Y_{n-1}^1$ follows a normal distribution $\mathcal{N}(\xi_{n-1}(X), \Sigma_{n-1}(X))$ where

$$\xi_{n-1}(X) = K(X, X_{n-1}^1)^\top K_{n-1}^{-1} Y_{n-1}^1, \quad \Sigma_{n-1}(X) = K(X, X) - K(X, X_{n-1}^1)^\top K_{n-1}^{-1} K(X, X_{n-1}^1). \quad (14)$$

In our landmarking algorithm, we simply choose X_n to be the location on the manifold M with the largest variance, i.e.

$$\begin{aligned} X_n &:= \underset{X \in M}{\operatorname{argmax}} \Sigma_{n-1}(X) \\ &= \underset{X \in M}{\operatorname{argmax}} \left[K(X, X) - K(X, X_{n-1}^1)^\top K_{n-1}^{-1} K(X, X_{n-1}^1) \right]. \end{aligned} \quad (15)$$

Notice that this successive procedure of “landmarking” X_1, X_2, \dots on M is independent of the specific choice of regression function in $\text{GP}(m, K)$ since we only need the covariance function $K : M \times M \rightarrow \mathbb{R}$.

We now describe the main algorithm of this paper, an unsupervised landmarking procedure for anatomical surfaces. Let M be a 2-dimensional compact surface isometrically embedded in \mathbb{R}^3 , and denote $\kappa : M \rightarrow \mathbb{R}$, $\eta : M \rightarrow \mathbb{R}$ for the Gaussian curvature and (scalar) mean curvature of M . Define a family of weight function $w_{\lambda, \rho} : M \rightarrow \mathbb{R}_{\geq 0}$ parametrized by $\lambda \in [0, 1]$ and $\rho > 0$ as

$$w_{\lambda, \rho}(x) = \frac{\lambda |\kappa(x)|^\rho}{\int_M |\kappa(\xi)|^\rho \, d\text{vol}_M(\xi)} + \frac{(1-\lambda) |\eta(x)|^\rho}{\int_M |\eta(\xi)|^\rho \, d\text{vol}_M(\xi)}, \quad \forall x \in M. \quad (16)$$

This weight function seeks to emphasize the influence of high curvature locations on the surface M on the covariance structure of the Gaussian process prior $\text{GP}(m, k_t^{w_{\lambda,\rho}})$, where $k_t^{w_{\lambda,\rho}}$ is the reweighted heat kernel defined in (11). For all applications discussed in this paper, we set $m \equiv 0$ but occasionally alter the parameters λ and ρ to fine-tune the landscape of the weight function (nevertheless, unless otherwise specified, we set by default $\lambda = 1/2$ and $\rho = 1$). For all practical purposes, we only concern ourselves with M being a piecewise linear surface, represented as a discrete triangular mesh $T = (V, E)$ with vertex set $V = \{x_1, \dots, x_{|V|}\} \subset \mathbb{R}^3$ and edge set E . We calculate the mean and Gaussian curvature functions η, κ on the triangular mesh (V, E) using standard algorithms in computational geometry [30, 3]. The weight function $w_{\lambda,\rho}$ can then be calculated at each vertex x_i by

$$w_{\lambda,\rho}(x_i) = \frac{\lambda |\kappa(x_i)|^\rho}{\sum_{k=1}^{|V|} |\kappa(x_k)|^\rho v(x_k)} + \frac{(1-\lambda) |\eta(x_i)|^\rho}{\sum_{k=1}^{|V|} |\eta(x_k)|^\rho v(x_k)}, \quad \forall x_i \in V \quad (17)$$

where $v(x_k)$ is the area of the Voronoi cell centered at x_i on the triangular mesh T . The reweighted heat kernel $k_t^{w_{\lambda,\rho}}$ is then defined on $V \times V$ as

$$k_t^{w_{\lambda,\rho}}(x_i, x_j) = \sum_{k=1}^{|V|} k_{t/2}(x_i, x_k) k_{t/2}(x_k, x_j) w_{\lambda,\rho}(x_k) v(x_k) \quad (18)$$

where the (unweighted) heat kernel k_t is calculated as in (9). Until a fixed total number of landmarks are collected, at each step k the algorithm computes the uncertainty score $\Sigma_{(k)}$ on V from the existing $(k-1)$ landmarks ξ_1, \dots, ξ_{k-1} by

$$\Sigma_{(k)}(x_i) = k_t^{w_{\lambda,\rho}}(x_i, x_i) - \begin{pmatrix} k_t^{w_{\lambda,\rho}}(x_i, \xi_1) \\ \vdots \\ k_t^{w_{\lambda,\rho}}(x_i, \xi_{k-1}) \end{pmatrix}^\top \begin{pmatrix} k_t^{w_{\lambda,\rho}}(\xi_1, \xi_1) & \cdots & k_t^{w_{\lambda,\rho}}(\xi_1, \xi_{k-1}) \\ \vdots & \ddots & \vdots \\ k_t^{w_{\lambda,\rho}}(\xi_{k-1}, \xi_1) & \cdots & k_t^{w_{\lambda,\rho}}(\xi_{k-1}, \xi_{k-1}) \end{pmatrix}^{-1} \begin{pmatrix} k_t^{w_{\lambda,\rho}}(x_i, \xi_1) \\ \vdots \\ k_t^{w_{\lambda,\rho}}(x_i, \xi_{k-1}) \end{pmatrix}, \quad \forall x_i \in V \quad (19)$$

and pick the k -th landmark ξ_k according to the rule

$$\xi_k = \operatorname{argmax}_{x_i \in V} \Sigma_{(k)}(x_i).$$

If there are more than one maximizers of $\Sigma^{(k)}$, we just randomly pick one; at step 1 the algorithm simply picks the vertex maximizing $x \mapsto k_t^{w_{\lambda,\rho}}(x, x)$ on V . See Algorithm 1 for a comprehensive description.

Remark 1. We require the inputs to be triangular meshes with edge connectivity only for the computation of discrete curvatures. This is not a hard constraint, though — many algorithms are readily available for computing curvatures on point clouds where the connectivity information is not present (see e.g. [119, 35]). Algorithm 1 can be easily adapted to use curvatures computed on point clouds as weights in the covariance function construction (11), which makes it applicable to a much wider range of input data accessible in geometric morphometrics; see Section 6.

Remark 2. Note that, according to (19), each step adds only one new row and one new column to the inverse covariance matrix, which enables us to perform rank-1 updates to the covariance matrix according to the block matrix inversion formula (see e.g. [113, §A.3])

$$K_n^{-1} = \begin{pmatrix} K_{n-1} & P \\ P^\top & K(X_n, X_n) \end{pmatrix}^{-1} = \begin{pmatrix} K_{n-1}^{-1} (I_{n-1} + \mu P P^\top K_{n-1}^{-1}) & -\mu K_{n-1}^{-1} P \\ -\mu P^\top K_{n-1}^{-1} & \mu \end{pmatrix}$$

where

$$P = \begin{pmatrix} K(X_1, X_n) \\ \vdots \\ K(X_{n-1}, X_n) \end{pmatrix} \in \mathbb{R}^{n-1}, \quad \mu = (K(X_n, X_n) - P^\top K_{n-1}^{-1} P)^{-1} \in \mathbb{R}.$$

This simple trick significantly improves the computational efficiency as it avoids directly inverting the covariance matrix when the number of landmarks becomes large as the iteration progresses.

Before we delve into the theoretical aspects of Algorithm 1, let us present a few typical instances of this algorithm in practical use. A more comprehensive evaluation of the applicability of Algorithm 1 to geometric morphometrics

Algorithm 1 GAUSSIAN PROCESS LANDMARKING WITH REWEIGHTED HEAT KERNEL

```

1: procedure GPL( $T, L, \lambda \in [0, 1], \rho > 0, \epsilon > 0$ ) ▷ Triangular Mesh  $T = (V, E)$ , number of landmarks  $L$ 
2:    $\kappa, \eta \leftarrow \text{DISCRETECURVATURES}(T)$  ▷ calculate discrete Gaussian curvature  $\kappa$  and mean curvature  $\eta$  on  $T$ 
3:    $v \leftarrow \text{VORONOIAREAS}(T)$  ▷ calculate the area of Voronoi cells around each vertex  $x_i$ 
4:    $w_{\lambda, \rho} \leftarrow \text{CALCULATEWEIGHT}(\kappa, \eta, \lambda, \rho, v)$  ▷ calculate weight function  $w_{\lambda, \rho}$  according to (17)
5:    $W \leftarrow \left[ \exp\left(-\|x_i - x_j\|^2 / \epsilon\right) \right]_{1 \leq i, j \leq |V|} \in \mathbb{R}^{|V| \times |V|}$ 
6:    $\Lambda \leftarrow \text{diag}\left(w_{\lambda, \rho}(x_1)v(x_1), \dots, w_{\lambda, \rho}(x_{|V|})v(x_{|V|})\right) \in \mathbb{R}^{|V| \times |V|}$ 
7:    $\xi_1, \dots, \xi_L \leftarrow \emptyset$  ▷ initialize landmark list
8:    $\Psi \leftarrow 0$ 
9:    $\ell \leftarrow 1$ 
10:   $K_{\text{full}} \leftarrow W^\top \Lambda W \in \mathbb{R}^{|V| \times |V|}$ 
11:   $K_{\text{trace}} \leftarrow \text{diag}(K_{\text{full}}) \in \mathbb{R}^{|V|}$ 
12:  while  $\ell < L + 1$  do
13:    if  $\ell = 1$  then
14:       $\Sigma \leftarrow K_{\text{trace}}$ 
15:    else
16:       $\Sigma \leftarrow K_{\text{trace}} - \text{diag}(\Psi^\top (\Psi [[\xi_1, \dots, \xi_\ell], :] \setminus \Psi)) \in \mathbb{R}^{|V|}$  ▷ calculate uncertainty scores by (19)
17:    end if
18:     $\xi_\ell \leftarrow \text{argmax } \Sigma$ 
19:     $\Psi \leftarrow K_{\text{full}}[:, [\xi_1, \dots, \xi_\ell]]$ 
20:     $\ell \leftarrow \ell + 1$ 
21:  end while
22:  return  $\xi_1, \dots, \xi_L$ 
23: end procedure

```

will be deferred to Section 6. In a nutshell, the Gaussian process landmarking algorithm picks the landmarks on the triangular mesh successively, according to the uncertainty score function Σ at the beginning of each step; at the end of each step the uncertainty score function gets updated, with the information of the newly picked landmark incorporated into the inverse covariance matrix defined as in (14). Figure 1 illustrates the first few successive steps on a triangular mesh discretization of a fossil molar of primate *Plesiadapoidea*. Empirically, we observed that the updates on the uncertainty score function are mostly local, i.e. no abrupt changes of the uncertainty score are observed away from a small geodesic neighborhoods centered at the new landmark. Guided by uncertainty and curvature-reweighted covariance function, the Gaussian process landmarking often identifies landmarks of abundant biological information—for instance, the first Gaussian process landmarks are often highly biologically informative, and demonstrate comparable level of coverage with the observer landmarks manually picked by human experts. See Figure 2 for a visual comparison between the automatically generated landmarks with the observer landmarks manually placed by evolutionary anthropologists on a different digitized fossil molar.

5 Convergence Analysis: Manifold Learning, Maximum Entropy Design, and Reduced Basis in Reproducing Kernel Hilbert Spaces

In this section, we provide some insights for the manifold landmarking algorithm proposed in Section 4 through several different lenses: Section 5.1 provides a pointwise convergence analysis for the reweighted kernel to the heat kernel of a Schoedinger operator; Section 5.2 relates Algorithm 1 to the near-optimal greedy strategy employed in maximum entropy experimental design; Section 5.3 establishes the rate of convergence for Algorithm 1 by bounding the decay of the conditional covariance in terms of the number of iterations. These analyses reveal the interplay among manifold learning, optimal experimental design, and reduced basis methods in partial differential equations.

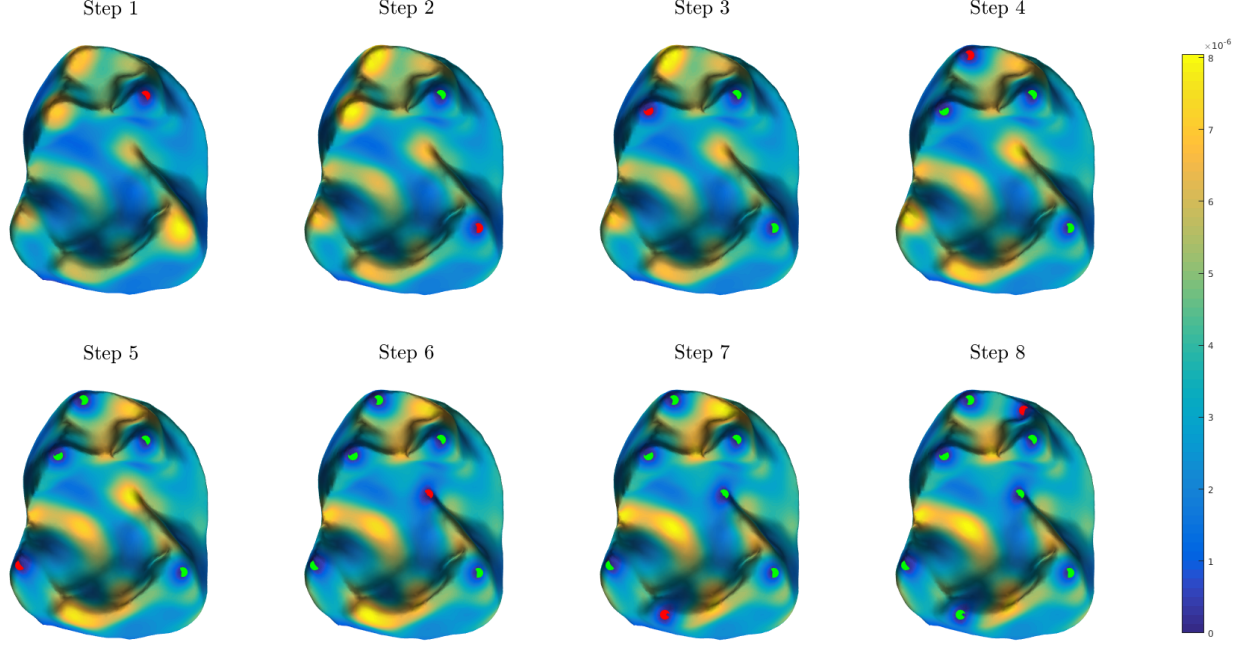


Figure 1: The first 8 landmarks picked successively by Gaussian Process Landmarking (Algorithm 1) on a digitized fossil molar of *Plesiadapoidea* (extinct mammals from the Paleocene and Eocene of North America, Europe, and Asia [128]), with the uncertainty scores at the end of each step rendered on the triangular mesh as a heat map. In each subfigure, the pre-existing landmarks are colored green, and the new landmark is colored red. At each step, the algorithm picks the vertex on the triangular mesh with the highest uncertainty score (computed according to (14)), then update the score function.

5.1 Pointwise Convergence of the Reweighted Kernel with Normalization

The reweighted kernel (11) is essential to the application of Algorithm 1 to geometric morphometrical applications. Intuitively, the reweighting step modifies the Euclidean heat kernel (9) by amplifying the influence of locations with relatively high weights, as suggested in (11) as well as its discretization (18). To investigate the role played by the reweighted kernel in greater detail, we study the behavior of the reweighed kernel in the asymptotic regime when the number of samples increases to infinity. To motivate Theorem 1 below, let us consider i.i.d. (with respect to the standard volume measure) samples $\{x_i\}_{i=1}^N$ on a closed Riemannian manifold (M, g) , as well as an arbitrary function $f \in C^2(M)$. To simplify the discussion, assume for the moment that the samples are uniformly distributed on M with respect to the normalized volume form on M . It is well known in manifold learning (see e.g. [130, 32]) that, for any $x \in M$,

$$\frac{1}{N} \sum_{j=1}^N \exp\left(-\frac{\|x - x_j\|^2}{2\epsilon}\right) f(x_j) \rightarrow \frac{1}{\text{Vol}(M)} \int_M \exp\left(-\frac{\|x - y\|^2}{2\epsilon}\right) f(y) \, d\text{Vol}(y) \quad \text{as } n \rightarrow \infty. \quad (20)$$

Denote the weight function used in (11) by

$$w(x) = e^{-V(x)}, \quad V(x) \geq 0 \quad \forall x \in M \quad (21)$$

since in our practice only non-negative weight functions $w \in C^2(M)$ are used, and typically we pick a normalization (e.g. in (17)) to ensure $0 \leq w \leq 1$ for numerical stability. Repeatedly using the “law of large numbers” argument (20), we have the following convergence for the reweighted kernel:

$$\begin{aligned} & \frac{1}{N^2} \sum_{k=1}^N \exp\left(-\frac{\|x - x_k\|^2}{2\epsilon}\right) \exp[-V(x_k)] \sum_{j=1}^N \exp\left(-\frac{\|x_k - x_j\|^2}{2\epsilon}\right) f(x_j) \rightarrow \\ & \frac{1}{[\text{Vol}(M)]^2} \int_M \int_M \exp\left(-\frac{\|x - z\|^2}{2\epsilon}\right) \exp[-V(z)] \exp\left(-\frac{\|z - y\|^2}{2\epsilon}\right) f(y) \, d\text{Vol}(z) \, d\text{Vol}(y) \quad \text{as } N \rightarrow \infty. \end{aligned}$$

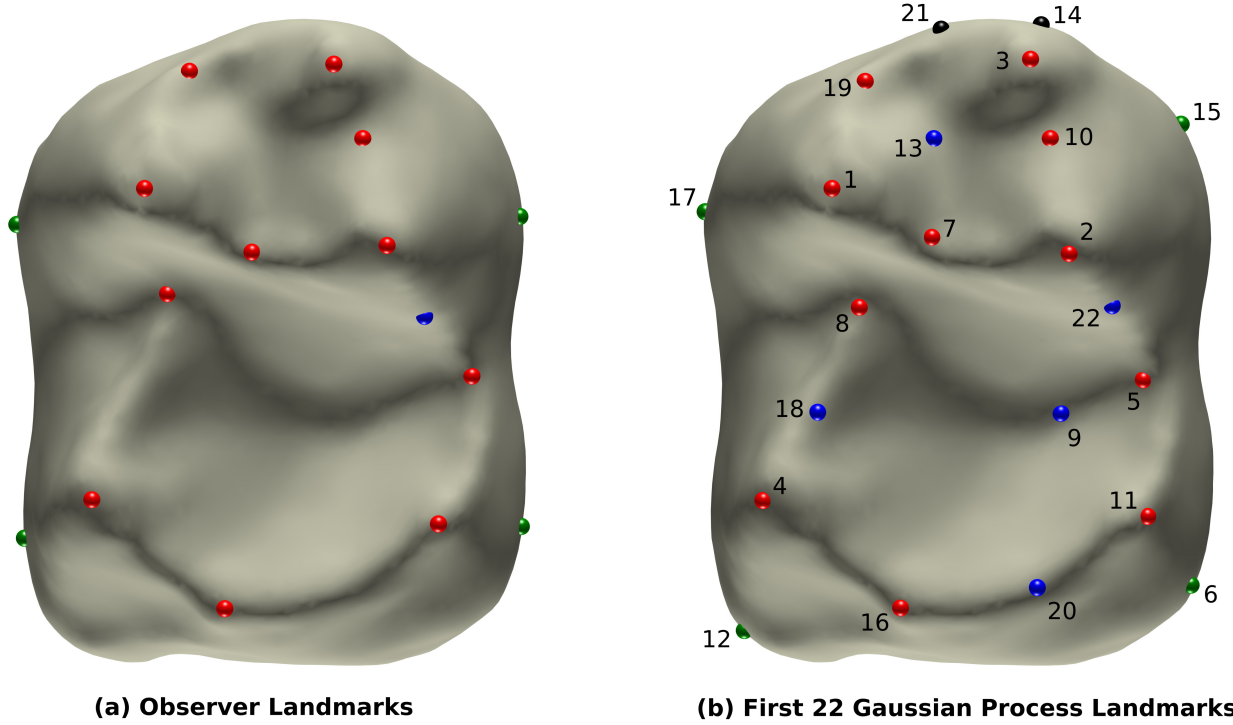


Figure 2: **Left:** Sixteen observer landmarks on a digitized fossil molar of a *Teilhardina* (one of the oldest known fossil primates closely related with living tarsiers and anthropoids [9]) identified manually by evolutionary anthropologists as ground truth, first published in [19]. **Right:** The first 22 landmarks picked by Gaussian Process Landmarking (Algorithm 1). The numbers next to each landmark indicate the order of appearance. The Gaussian process landmarks strikingly resembles the observer landmarks: the red landmarks (Number 1-5, 7, 8, 10, 11, 16, 19) signals geometric sharp features (cusps or saddle points corresponding to local maximum/minimum Gaussian curvature); the blue landmarks sit either along the curvy cusp ridges and grooves (Number 13, 18, 20, 22) or at the basin (Number 9), serving the role often played by semilandmarks; the four green landmarks (Number 6, 12, 15, 17) approximately delimit the “outline” of the tooth in occlusal view.

This motivates us to consider the asymptotic behavior of the integral operator on the right hand side in the asymptotic regime $\epsilon \rightarrow \infty$, a recurring theme in manifold learning (see e.g. [10, 32, 131, 43]).

Theorem 1. *Let M be a d -dimensional closed manifold. For any $f, V \in C^\infty(M)$ and $V \geq 0$,*

$$\frac{\int_M \int_M \exp\left(-\frac{\|x-z\|^2}{2\epsilon}\right) \exp[-V(z)] \exp\left(-\frac{\|z-y\|^2}{2\epsilon}\right) f(y) \, d\text{Vol}(z) \, d\text{Vol}(y)}{\int_M \int_M \exp\left(-\frac{\|x-z\|^2}{2\epsilon}\right) \exp[-V(z)] \exp\left(-\frac{\|z-y\|^2}{2\epsilon}\right) \, d\text{Vol}(z) \, d\text{Vol}(y)} \quad (22)$$

$$\longrightarrow f(x) + \epsilon \left(\Delta f(x) - \nabla f(x) \cdot \nabla V(x) \right) + O\left(\epsilon^{\frac{3}{2}}\right) \quad \text{as } \epsilon \rightarrow 0.$$

The proof of Theorem 1 can be found in Appendix A. Theorem 1 indicates that a proper normalization of the reweighted kernel (11) gives rise to an approximation to the heat kernel of the backward Kolmogorov operator

$$L = -\Delta + \nabla V \cdot \nabla.$$

Note that this operator is also the infinitesimal generator of the diffusion process determined by stochastic differential equation

$$dX_t = -\nabla V(X_t) \, dt + \sqrt{2} \, dW_t$$

where W_t is the standard Wiener process defined on M . In particular, Theorem 1 suggests that our construction of the reweighted kernel encodes information from the weight function into the dynamics of the stochastic process on M .

Remark 3. It is interesting to compare the result of Theorem 1 with the related but different kernel construction in diffusion maps [32, 94]. The integral operator in (22) is a properly normalized version of integration a smooth function against the kernel

$$\tilde{K}_V(x, y) := \int_M \exp\left(-\frac{\|x-z\|^2}{2\epsilon}\right) \exp[-V(z)] \exp\left(-\frac{\|z-y\|^2}{2\epsilon}\right) d\text{Vol}(z)$$

which is obtained from sandwiching $\exp[-V(\cdot)]$ with the squared exponential kernel. If we pick a different order of sandwiching, namely, construct the kernel as

$$K_V(x, y) := \exp[-V(x)] \exp\left(-\frac{\|x-y\|^2}{2\epsilon}\right) \exp[-V(y)],$$

then a quick computation in the same spirit as [14, Theorem 1] leads to

$$\frac{\int_M K_V(x, y) f(y) d\text{vol}_M(y)}{\int_M K_V(x, y) d\text{vol}_M(y)} \longrightarrow f(x) + \epsilon \left(\frac{1}{2} \Delta f(x) - \nabla f(x) \cdot \nabla V(x) \right) + O(\epsilon^{\frac{3}{2}}) \quad \text{as } \epsilon \rightarrow 0.$$

In other words, the infinitesimal generator differs from the one calculated in (22) only by an additional scalar factor in front of the Laplace-Beltrami operator. Indeed, we observe very similar numerical results when replacing \tilde{K}_V with K_V in Algorithm 1. Empirical evidence motivates us to conjecture that the subtlety between using \tilde{K}_V and K_V in the landmarking algorithm lies mainly at the choice of the bandwidth parameter, but a deeper investigation of the statistical performance with respect to the choice of bandwidth is beyond the scope of the current paper.

The behavior of the kernel becomes even more interesting if we let the weight function depend on the bandwidth parameter $\epsilon > 0$ as well. For instance, if we replace (21) by

$$w_\epsilon(x) = e^{-V(x)/\epsilon}, \quad V(x) \geq 0 \quad \forall x \in M \quad (23)$$

then the integral operator considered in Theorem 1 is replaced with

$$T_\epsilon f(x) := \frac{1}{[\text{Vol}(M)]^2} \int_M \int_M \exp\left(-\frac{\|x-z\|^2}{2\epsilon}\right) \exp\left[-\frac{V(z)}{\epsilon}\right] \exp\left(-\frac{\|z-y\|^2}{2\epsilon}\right) f(y) d\text{Vol}(z) d\text{Vol}(y), \quad \forall f \in C^2(M). \quad (24)$$

An almost identical calculation as in the proof of Theorem 1 leads to

Corollary 1. Under the same assumptions as in Theorem 1,

$$\frac{\int_M \int_M \exp\left(-\frac{\|x-z\|^2}{2\epsilon}\right) \exp\left[-\frac{V(z)}{\epsilon}\right] \exp\left(-\frac{\|z-y\|^2}{2\epsilon}\right) f(y) d\text{Vol}(z) d\text{Vol}(y)}{\int_M \int_M \exp\left(-\frac{\|x-z\|^2}{2\epsilon}\right) \exp\left[-\frac{V(z)}{\epsilon}\right] \exp\left(-\frac{\|z-y\|^2}{2\epsilon}\right) d\text{Vol}(z) d\text{Vol}(y)} \longrightarrow f(x) + \epsilon \left(\Delta f(x) - \nabla f(x) \cdot \frac{1}{\epsilon} \nabla V(x) \right) + O(\epsilon^{\frac{3}{2}}) \quad \text{as } \epsilon \rightarrow 0. \quad (25)$$

Similar to Theorem 1, Corollary 1 shows that a proper normalization of the kernel reweighted by (23) approximates the heat kernel of the operator

$$L_\epsilon := -\Delta + \frac{1}{\epsilon} \nabla V \cdot \nabla.$$

The dependence on ϵ is of particular interest. It is well known in the literature of semi-classical analysis that ϵL_ϵ is conjugate to the Witten Laplacian on 0-forms:

$$\Delta_{V,\epsilon} = \epsilon e^{-V/2\epsilon} (\epsilon L_\epsilon) e^{V/2\epsilon}$$

where

$$\Delta_{V,\epsilon} = -\epsilon^2 \Delta + \frac{1}{4} |\nabla V|^2 - \frac{\epsilon}{2} \Delta V.$$

Since the eigenfunctions of $\Delta_{V,\epsilon}$ corresponding to the leading small eigenvalues concentrate near the critical points of the potential function V for sufficiently small $\epsilon > 0$ (see e.g. [64] or [105, Theorem 3.9]), the eigenfunctions corresponding to the leading small eigenvalues of L_ϵ also concentrate near the critical points of V after being multiplied by $e^{-V/2\epsilon}$, which, by the proof of Theorem 1, can be approximated by the square root of the denominator of (25). Note that the matrix K_{full} in Algorithm 1 corresponds to the integral kernel in the numerator of (25) if we choose Λ to be the diagonal matrix with $\exp[-V(v_i)/\epsilon]$ at its i -th diagonal entry, where v_i is the i -th vertex on the triangular mesh; setting D to be the diagonal matrix with the i -th row sum of K_{full} at its i -th diagonal entry, the Witten Laplacian $\Delta_{V,\epsilon}$ can then be approximated using

$$D^{-1/2} K_{\text{full}} D^{-1/2}$$

up to a scalar multiplication by the bandwidth ϵ . We would thus expect the first few eigenfunctions corresponding to the smallest eigenvalues of $D^{-1/2} K_{\text{full}} D^{-1/2}$ to concentrate near the critical points of V . This can be easily verified with numerical experiments; see Figure 3 for an example.

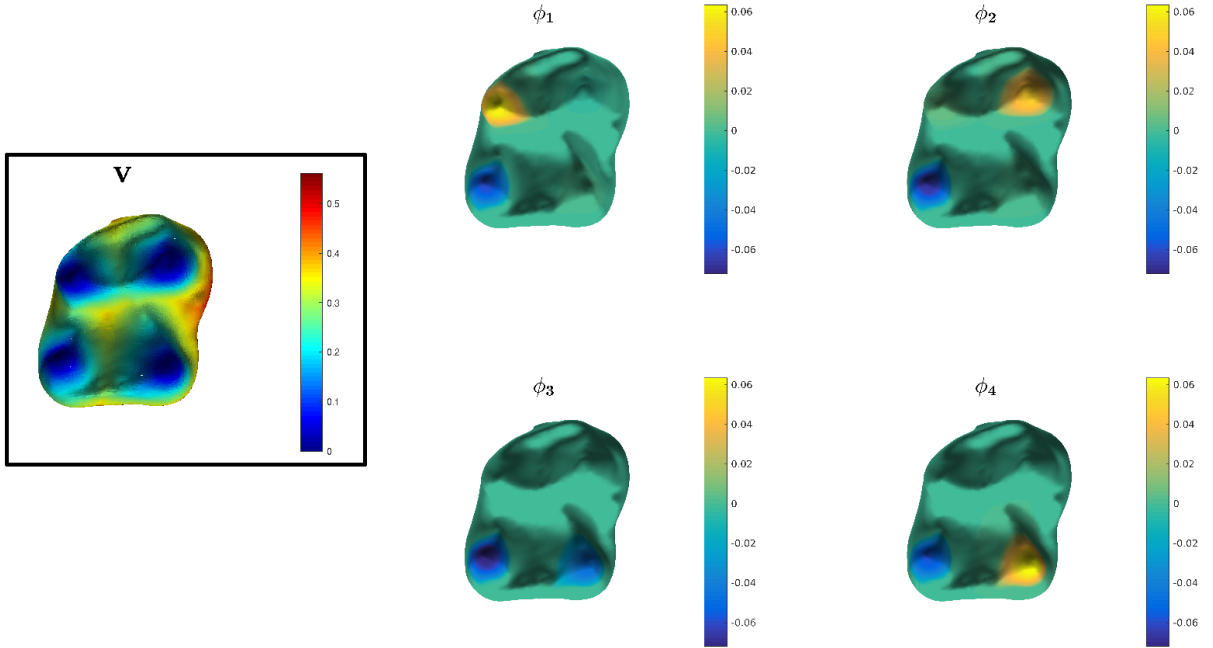


Figure 3: Concentration of the eigenfunctions of the Witten Laplacian with respect to a potential function V . The left boxed subplot illustrates the potential function V using a heat map; we constructed this potential to have 4 wells centered around 4 cusps manually picked on a *Lorisidae* mandibular molar. The 4 eigenfunctions corresponding to the 4 smallest eigenvalues of the Witten Laplacian with potential V are depicted on the 2×2 panel on the right; it can be read off from the colorbars that the support of each of these 4 eigenfunctions are concentrated around critical points of V . See Section 5.1 for more details.

Remark 4. *The localization effects on eigenfunctions can also be achieved by adding a diagonal matrix, which represents a potential function on the domain of interest, to the kernel matrix; this idea has found applications in biomedical data analysis [36] and computer graphics [88]. The insight we gained from relating the reweighted kernel to Witten Laplacian reveals that the localization can be equivalently realized through a simple nonlinear procedure motivated. This coincidence can be explained as follows: while adding a diagonal potential to the kernel provides a direct discretization of the Schrödinger operator $L_V = -\Delta + V$, the reweighted kernel (12) can be thought of as a discretization of the heat kernel of L_V by taking only “one-hop” paths in the Feynmann-Kac formula for e^{-tL_V} . An extensive discussion along this direction is beyond the scope of the current paper; interested readers may find useful the works [134, 135, 58] and the references therein.*

The connection between the reweighted kernel (11) and the semi-classical analysis of the Witten Laplacian provides insights for the behavior of the Gaussian process landmarks generated from Algorithm 1. Given a Gaussian

process $\text{GP}(m, K)$ defined on a manifold M , the eigenfunctions of K —properly reweighted by their corresponding eigenvalues—gives rise to the Karhunen-Loève basis for $\text{GP}(m, K)$, with respect to which the sample paths of $\text{GP}(m, K)$ adopt expansions with i.i.d. standard normal coefficients. If the low-frequency components of these expansions tend to concentrate at certain regions on M , when fitting an unknown function in $\text{GP}(m, K)$ using an active learning procedure, it could be much more efficient if one begins with the inquiry for the function value at those regions of concentration. After information at regions of concentration are collected to some extent, it becomes necessary to search for clues filling up the complement on M of those concentration regions. Therefore, spreading landmarks on M using a Gaussian process with reweighted kernel balances out the information contained in the landscape of the weight function and the space-filling experimental design strategies. Another advantage of not selecting landmarks solely based on the weight function is that the weight function can be too spurious to produce reliable, semantically meaningful landmarks, at least for our application in geometric morphometrics; see Figure 4 for an example for such a comparison.

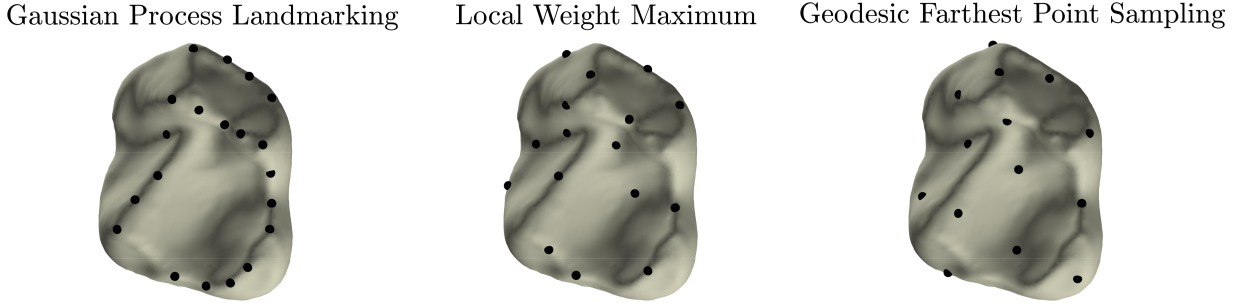


Figure 4: **Left:** Gaussian process landmarks generated using Algorithm 1 with a exponential squared kernel function reweighted by weight function w ; **Middle:** The local maxima of the weight function used in the reweighed kernel, which appears semantically less meaningful from the perspective of geometric morphometrics; **Right:** Points produced by the *geodesic farthest point sampling* (see e.g. [52, 91]), a greedy algorithm common used for generating uniformly sampled (or approximately space-filling) points on a triangular mesh. Comparing these three sampling approaches, Gaussian process landmarks has the advantage of tending to fill up the manifold while prioritizing the choice of semantically meaningful features for geometric morphometrics.

5.2 Near-Optimality of Gaussian Process Landmarking as Maximum Entropy Design

Algorithm 1 greedily picks the point on the manifold M that maximizes the conditional variance as the next landmark. This sequential optimization approach is reminiscent of a popular approximation scheme in entropy-based experimental design [73, 100, 122]. The key observation here is the equivalence between minimizing the *conditional entropy* (or maximizing the *information gain*) and maximizing the determinant of the conditional covariance matrix; see e.g. [122, §6.2.1], [73, §3.1], [100, §2.2]. More concretely, if we denote the maximum entropy of a Gaussian process $\text{GP}(m, K)$ on a manifold M with respect to any n observations as

$$\text{OPT}(n) := \max_{\{x_1, \dots, x_n\} \subset M} \det K(x_1, \dots, x_n)$$

where $K(x_1, \dots, x_n)$ is defined in (13), and

$$\text{GPL}(n) := \det K(X_1, \dots, X_n) \quad \text{where } X_1, \dots, X_n \text{ are generated using Algorithm 1}$$

then by the *submodularity* of the entropy function [69] we conclude, using classic results [97], that

$$\text{OPT}(n) \geq \text{GPL}(n) \geq (1 - 1/e) \text{OPT}(n).$$

In other words, the entropy of the greedy algorithm is equivalent to the maximum entropy up to a multiplicative constant. We point out that this justifies the information-theoretic asymptotic near-optimality of Gaussian Process Landmarking (Algorithm 1).

5.3 Rate of Convergence: A Connection with Reduced Basis Methods in Reproducing Kernel Hilbert Spaces

In this subsection we analyze the rate of convergence of our main Gaussian process landmarking algorithm in Section 4. While the notion of “convergence rate” in the context of Gaussian process regression (i.e. *kriging* [93, 137]) or scattered data approximation (see e.g. [145] and the references therein) refers to how fast the interpolant approaches the true function, our focus in this paper is the rate of convergence of Algorithm 1 itself, for instance, the number of steps the algorithm takes before it terminates. In practice, unless a maximum number of landmarks is predetermined, a natural criterion for terminating the algorithm is to specify a threshold for the ∞ -norm of the conditional covariance (15) over the manifold. We emphasize again that, although this greedy approach is motivated by the probabilistic model of Gaussian processes, the conditional covariance function as well as the greedy algorithm of manifold landmarking is completely deterministic once the kernel function is known. Our analysis is thus centered around bounding the uniform rate at which the conditional covariance decays with respect to number landmarks greedily selected.

To this end, we observe the connection between Algorithm 1 and a greedy algorithm studied thoroughly for *reduced basis methods* in [16, 37] in the context of model reduction. While the analyses in [16, 37] assume general Hilbert and Banach spaces, we apply their result to a reproducing kernel Hilbert space (RKHS), denoted as \mathcal{H}_K , naturally associated with a Gaussian process $\text{GP}(m, K)$; as will be demonstrated below, the conditional covariance function with respect to n selected landmarks can be interpreted as a distance function between elements of \mathcal{H}_K to an n -dimensional subspace of \mathcal{H}_K determined by the selected landmarks. We emphasize that, though the connection between Gaussian process and RKHS is well known (see e.g. [142] and the references therein), we are not aware of existing literature addressing the resemblance between the two classes of greedy algorithms widely used in Gaussian process experimental design and reduced basis methods.

We begin with a brief summary of the greedy algorithm in reduced basis methods for a general Banach space $(X, \|\cdot\|)$. The algorithm strives to approximate *all* elements of X using a properly constructed linear subspace spanned by (as few as possible) selected elements from a compact subset $\mathcal{F} \subset X$; thus the name “reduced” basis. A popular greedy algorithm for this purpose generates successive approximation spaces by choosing the first basis $f_1 \in \mathcal{F}$ according to

$$f_1 := \operatorname{argmax}_{f \in \mathcal{F}} \|f\| \quad (26)$$

and, successively, when f_1, \dots, f_{n-1} are picked already, choose

$$f_{n+1} := \operatorname{argmax}_{f \in \mathcal{F}} \operatorname{dist}(f, V_n) \quad (27)$$

where

$$V_n = \operatorname{span}\{f_1, f_2, \dots, f_n\}$$

and

$$\operatorname{dist}(f, V_n) := \inf_{g \in V_n} \|f - g\|.$$

In words, at each step we greedily pick the function that is “farthest away” from the set of already chosen basis elements. Intuitively, this is a Banach space analogy of the farthest point sampling algorithm [52, 91] already mentioned in Section 5.1. To fit Gaussian process landmarking into this framework, let us first specialize this construction to the case when X is the reproducing kernel Hilbert space $\mathcal{H}_K \subset L^2(M)$, where M is a compact Riemannian manifold and K is the reproducing kernel. A natural choice for K is the heat kernel $k_t(\cdot, \cdot) : M \times M \rightarrow \mathbb{R}$ with a fixed $t > 0$ as in Section 2.1, but for a submanifold isometrically embedded into an ambient Euclidean space it is common as well to choose the kernel to be the restriction to M of a positive (semi-)definite kernel in the ambient Euclidean space such as (9) or (12), for which Sobolev-type error estimates are known in the literature of scattered data approximation [96, 41]. It follows from standard RKHS theory that

$$\mathcal{H}_K = \overline{\operatorname{span}\left\{\sum_{i \in I} a_i K(\cdot, x_i) \mid a_i \in \mathbb{R}, x_i \in M, \operatorname{card}(I) < \infty\right\}} \quad (28)$$

and, by the compactness of M and the regularity of the kernel function, we have for any $x \in M$

$$\langle K(\cdot, x), K(\cdot, x) \rangle_{\mathcal{H}_K} = K(x, x) \leq \|K\|_{\infty, M \times M} < \infty$$

which justifies the compactness of

$$\mathcal{F} := \text{span} \{K(\cdot, x) \mid x \in M\} \quad (29)$$

as a subset of \mathcal{H}_K . In fact, since we only used the compactness of M and the boundedness of K on $M \times M$, the argument above for the compactness of \mathcal{F} can be extended to any Gaussian process defined on a compact metric space with a bounded kernel. The initialization step (26) now amounts to selecting $K(\cdot, x)$ from \mathcal{F} that maximizes

$$\|K(\cdot, x)\|_{\mathcal{H}_K}^2 = \langle K(\cdot, x), K(\cdot, x) \rangle_{\mathcal{H}_K} = K(x, x)$$

which is identical to (15) when $n = 1$ (or equivalently, Line 14 in Algorithm 1); furthermore, given $n \geq 1$ previously selected basis functions $K(\cdot, x_1), \dots, K(\cdot, x_n)$, the $(n+1)$ -th basis function will be chosen according to (27), i.e. $f_{n+1} = K(\cdot, x_n)$ maximizes the infimum

$$\begin{aligned} \inf_{g \in \text{span}\{K(\cdot, x_1), \dots, K(\cdot, x_n)\}} \|K(\cdot, x) - g\|_{\mathcal{H}_K}^2 &= \inf_{a_1, \dots, a_n \in \mathbb{R}} \left\| K(\cdot, x) - \sum_{i=1}^n a_i K(\cdot, x_i) \right\|_{\mathcal{H}_K}^2 \\ &= \inf_{a_1, \dots, a_n \in \mathbb{R}} K(x, x) - 2 \sum_{i=1}^n a_i K(x, x_i) + \sum_{i=1}^n \sum_{j=1}^n a_i a_j K(x_i, x_j) \\ &\stackrel{(*)}{=} K(x, x) - 2 \begin{pmatrix} K(x, x_1) & \cdots & K(x, x_n) \end{pmatrix} \begin{pmatrix} K(x_1, x_1) & \cdots & K(x_1, x_n) \\ \vdots & & \vdots \\ K(x_n, x_1) & \cdots & K(x_n, x_n) \end{pmatrix}^{-1} \begin{pmatrix} K(x, x_1) \\ \vdots \\ K(x, x_n) \end{pmatrix} \\ &\quad + \begin{pmatrix} K(x, x_1) & \cdots & K(x, x_n) \end{pmatrix} \begin{pmatrix} K(x_1, x_1) & \cdots & K(x_1, x_n) \\ \vdots & & \vdots \\ K(x_n, x_1) & \cdots & K(x_n, x_n) \end{pmatrix}^{-1} \begin{pmatrix} K(x, x_1) \\ \vdots \\ K(x, x_n) \end{pmatrix} \\ &= K(x, x) - \begin{pmatrix} K(x, x_1) & \cdots & K(x, x_n) \end{pmatrix} \begin{pmatrix} K(x_1, x_1) & \cdots & K(x_1, x_n) \\ \vdots & & \vdots \\ K(x_n, x_1) & \cdots & K(x_n, x_n) \end{pmatrix}^{-1} \begin{pmatrix} K(x, x_1) \\ \vdots \\ K(x, x_n) \end{pmatrix} \quad (30) \end{aligned}$$

where the equality $(*)$ follows from the observation that, for any fixed $x \in M$, the minimizing vector $(a_1, \dots, a_n) \in \mathbb{R}^n$ satisfies

$$\begin{aligned} \begin{pmatrix} K(x, x_1) \\ \vdots \\ K(x, x_n) \end{pmatrix} &= \begin{pmatrix} K(x_1, x_1) & \cdots & K(x_1, x_n) \\ \vdots & & \vdots \\ K(x_n, x_1) & \cdots & K(x_n, x_n) \end{pmatrix} \begin{pmatrix} a_1 \\ \vdots \\ a_n \end{pmatrix} \\ \Leftrightarrow \begin{pmatrix} a_1 \\ \vdots \\ a_n \end{pmatrix} &= \begin{pmatrix} K(x_1, x_1) & \cdots & K(x_1, x_n) \\ \vdots & & \vdots \\ K(x_n, x_1) & \cdots & K(x_n, x_n) \end{pmatrix}^{-1} \begin{pmatrix} K(x, x_1) \\ \vdots \\ K(x, x_n) \end{pmatrix}. \end{aligned}$$

It is clear at this point that maximizing the rightmost quantity in (30) is equivalent to following the greedy landmark selection criterion (15) at the $(n+1)$ -th step. We thus conclude that Algorithm 1 is equivalent to the greedy algorithm for reduced basis method in \mathcal{H}_K , a reproducing kernel Hilbert space modeled on the compact manifold M . The following lemma summarizes this observation for future reference.

Lemma 1. *Let M be a compact Riemannian manifold, and let $K : M \times M \rightarrow \mathbb{R}$ be a positive semidefinite kernel function. Consider the reproducing kernel Hilbert space $\mathcal{H}_K \subset L^2(M)$ as defined in (28). For any $x \in M$ and a collection of n points $\mathcal{X}_n = \{x_1, x_2, \dots, x_n\} \subset M$, the orthogonal projection P_n from \mathcal{H}_K to $V_n = \text{span} \{K(\cdot, x_i) \mid 1 \leq i \leq n\}$ is*

$$P_n(K(\cdot, x)) = \sum_{i=1}^n a_i^*(x) K(\cdot, x_i)$$

where $a_i^* : M \rightarrow \mathbb{R}$ is the inner product of $(K(x, x_1), \dots, K(x, x_n))$ with the i -th row of

$$\begin{pmatrix} K(x_1, x_1) & \cdots & K(x_1, x_n) \\ \vdots & & \vdots \\ K(x_n, x_1) & \cdots & K(x_n, x_n) \end{pmatrix}^{-1}.$$

In particular, a_i^* has the same regularity as the kernel Φ , for all $1 \leq i \leq n$. Moreover, the squared distance between $K(\cdot, x)$ and the linear subspace $V_n \subset \mathcal{H}_K$ has the closed-form expression

$$\begin{aligned}
P_{K, \mathcal{X}_n}(x) &:= \|K(\cdot, x) - P_n(K(\cdot, x))\|_{\mathcal{H}_K}^2 \\
&= \min_{a_1, \dots, a_n \in \mathbb{R}} \left\| K(\cdot, x) - \sum_{i=1}^n a_i K(\cdot, x_i) \right\|_{\mathcal{H}_K}^2 \\
&= K(x, x) - \left(K(x, x_1), \dots, K(x, x_n) \right) \begin{pmatrix} K(x_1, x_1) & \cdots & K(x_1, x_n) \\ \vdots & & \vdots \\ K(x_n, x_1) & \cdots & K(x_n, x_n) \end{pmatrix}^{-1} \begin{pmatrix} K(x, x_1) \\ \vdots \\ K(x, x_n) \end{pmatrix}.
\end{aligned} \tag{31}$$

Consequently, for any Gaussian process defined on M with covariance structure given by the kernel function K , the conditional covariance of the Gaussian process conditioned on the observations at $x_1, \dots, x_n \in M$ equals to the distance between $K(\cdot, x)$ and the subspace V_n spanned by $K(\cdot, x_1), \dots, K(\cdot, x_n)$.

The function $P_{K, \mathcal{X}_n} : M \rightarrow \mathbb{R}_{\geq 0}$ defined in (31) is in fact the squared *power function* in the literature of scattered data approximation; see e.g. [145, Definition 11.2].

The convergence rate of greedy algorithms for reduced basis methods has been investigated in a series of works [23, 16, 37]. The general paradigm is to compare the maximum approximation error incurring after the n -th greedy step, denoted as

$$\sigma_n := \text{dist}(f_{n+1}, V_n) = \max_{f \in \mathcal{F}} \text{dist}(f, V_n),$$

with the *Kolmogorov width* (c.f. [83]), a quantity characterizing the theoretical optimal error of approximation using any n -dimensional linear subspace generated from any greedy or non-greedy algorithms, defined as

$$d_n := \inf_Y \sup_{f \in \mathcal{F}} \text{dist}(f, Y)$$

where the first infimum is taken over all n -dimensional subspaces Y of X . When $n = 1$, both σ_1 and d_1 degenerate to the ∞ -bound of the kernel function on $M \times M$, i.e. $\|K\|_{\infty, M \times M}$. In [37] the following comparison between $\{\sigma_n \mid n \in \mathbb{N}\}$ and $\{d_n \mid n \in \mathbb{N}\}$ was established:

Theorem 2 ([37], Theorem 3.2 (The $\gamma = 1$ Case)). *For any $N \geq 0$, $n \geq 1$, and $1 \leq m < n$, there holds*

$$\prod_{\ell=1}^n \sigma_{N+\ell}^2 \leq \left(\frac{n}{m} \right)^m \left(\frac{n}{n-m} \right)^{n-m} \sigma_{N+1}^{2m} d_m^{2n-2m}.$$

This result establishes the asymptotic optimality of the greedy basis selection procedure. In particular, setting $N = 0$ and taking advantage of the monotonicity of the sequence $\{\sigma_n \mid n \in \mathbb{N}\}$, one has from Theorem 2 that

$$\sigma_n \leq \sqrt{2} \min_{1 \leq m < n} \|K\|_{\infty, M \times M}^{\frac{m}{n}} d_m^{\frac{n-m}{n}}$$

for all $n \in \mathbb{N}$. Using the monotonicity of $\{\sigma_n \mid n \in \mathbb{N}\}$, by setting $m = \lfloor n/2 \rfloor$ we have the even more compact inequality

$$\sigma_n \leq \sqrt{2} \|K\|_{\infty, M \times M}^{\frac{1}{2}} d_{\lfloor n/2 \rfloor}^{\frac{1}{2}} \quad \text{for all } n \in \mathbb{N}. \tag{32}$$

If we have an asymptotic bound for $\{d_n \mid n \in \mathbb{N}\}$ (in the regime $n \rightarrow \infty$), inequality (32) can be invoked to establish an asymptotic bound for $\{\sigma_n \mid n \in \mathbb{N}\}$. We emphasize here that the definition of $\{d_n \mid n \in \mathbb{N}\}$ only involves those elements in a compact subset \mathcal{F} of the ambient Hilbert space \mathcal{H}_K ; in our setting, the compact subset (29) consists of only functions of the form $K(\cdot, x)$ for some $x \in M$, thus

$$\begin{aligned}
d_n &= \inf_{x_1, \dots, x_n \in M} \sup_{x \in M} \text{dist}(K(\cdot, x), \text{span}\{K(\cdot, x_i) \mid 1 \leq i \leq n\}) \\
&= \inf_{x_1, \dots, x_n \in M} \sup_{x \in M} \left[K(x, x) - \left(K(x, x_1), \dots, K(x, x_n) \right) \begin{pmatrix} K(x_1, x_1) & \cdots & K(x_1, x_n) \\ \vdots & & \vdots \\ K(x_n, x_1) & \cdots & K(x_n, x_n) \end{pmatrix}^{-1} \begin{pmatrix} K(x, x_1) \\ \vdots \\ K(x, x_n) \end{pmatrix} \right].
\end{aligned} \tag{33}$$

To ease notation, we will always denote $\mathcal{X}_n := \{x_1, \dots, x_n\}$ as in Lemma 1. Write the maximum value of the function P_{K, \mathcal{X}_n} over M as

$$\Pi_{K, \mathcal{X}_n} := \sup_{x \in M} P_{K, \mathcal{X}_n}(x). \quad (34)$$

The Kolmogorov width d_n can be put in these notations as

$$d_n = \inf_{x_1, \dots, x_n \in M} \Pi_{K, \mathcal{X}_n}. \quad (35)$$

The problem of bounding $\{d_n \mid n \in \mathbb{N}\}$ thus reduces to bounding the infimum of Π_{K, \mathcal{X}_n} over all n -dimensional linear subspaces of \mathcal{F} .

When M is an open, bounded subset of a standard Euclidean space, upper bounds for Π_{K, \mathcal{X}_n} are often established—in a kernel-adaptive fashion—using the *fill distance* [145, Chapter 11]

$$h_{\mathcal{X}_n} := \sup_{x \in M} \min_{x_j \in \mathcal{X}_n} \|x - x_j\| \quad (36)$$

where $\|\cdot\|$ is the Euclidean norm of the ambient space. For instance, when K is a squared exponential kernel (9) and the domain is a cube (at least compact and convex, as pointed out in [144, Theorem 1]) in a Euclidean space, [145, Theorem 11.22] asserts that

$$\Pi_{K, \mathcal{X}_n} \leq \exp \left[c \frac{\log h_{\mathcal{X}_n}}{h_{\mathcal{X}_n}} \right] \quad \forall h_{\mathcal{X}_n} \leq h_0 \quad (37)$$

for some constants $c > 0, h_0 > 0$ depending only on M and the kernel bandwidth $t > 0$ in (9). Similar bounds have been established in [147] for Matérn kernels, but the convergence rate is only polynomial. In this case, by the monotonicity of the function $x \mapsto \log x/x$ for $x \in (0, e)$, we have, for all sufficiently small $h_{\mathcal{X}_n}$,

$$d_n = \inf_{x_1, \dots, x_n \in M} \Pi_{K, \mathcal{X}_n} \leq \exp \left[c \frac{\log h_n}{h_n} \right]$$

where

$$h_n := \inf_{\mathcal{X}_n \subset M, |\mathcal{X}_n|=n} h_{\mathcal{X}_n} \quad (38)$$

is the minimum fill distance attainable for any n sample points on M . We thus have the following theorem for the convergence rate of Algorithm 1 for any compact, convex set in a Euclidean spaces:

Theorem 3. *Let $\Omega \subset \mathbb{R}^D$ be a compact and convex subset of the D -dimensional Euclidean space, and consider a Gaussian process $\text{GP}(m, K)$ defined on Ω , with the covariance function K being of the squared exponential form (9) with respect to the ambient D -dimensional Euclidean distance. Let X_1, X_2, \dots denote the sequence of landmarks greedily picked on Ω according to Algorithm 1, and define for any $n \in \mathbb{N}$ the maximum conditional covariance on Ω with respect to the first n landmarks X_1, \dots, X_n as*

$$\sigma_n = \max_{x \in \Omega} \left[K(x, x) - \left(K(x, X_1), \dots, K(x, X_n) \right) \begin{pmatrix} K(X_1, X_1) & \dots & K(X_1, X_n) \\ \vdots & & \vdots \\ K(X_n, X_1) & \dots & K(X_n, X_n) \end{pmatrix}^{-1} \begin{pmatrix} K(x, X_1) \\ \vdots \\ K(x, X_n) \end{pmatrix} \right].$$

Then

$$\sigma_n = O\left(\beta^{\frac{\log h_n}{h_n}}\right) \quad \text{as } h_n \rightarrow 0 \quad (39)$$

for some positive constant $\beta > 1$ depending only on the geometry of the domain Ω and the bandwidth of the squared exponential kernel K ; h_n is the minimum fill distance of n arbitrary points on Ω (c.f. (38)).

Proof. By the monotonicity of the sequence $\{\sigma_n \mid n \in \mathbb{N}\}$, it suffices to establish the convergence rate for a subsequence. Using directly (32), (35), (37), and the definition of h_n in (38), we have the inequality

$$\sigma_{2n} \leq \sqrt{2} \|K\|_{\infty, \Omega \times \Omega}^{\frac{1}{2}} \exp \left[\frac{c \log h_n}{2 h_n} \right] = \sqrt{2} \|K\|_{\infty, \Omega \times \Omega}^{\frac{1}{2}} \beta^{\frac{\log h_n}{h_n}} \quad \text{where } \beta := \exp(c/2) > 1$$

for all $\mathbb{N} \ni n \geq N$. Here the positive constants $N = N(\Omega, t) > 0$ and $c = c(\Omega, t) > 0$ depend only on the geometry of Ω and the bandwidth of the squared exponential kernel. This completes the proof. \square

Convex bodies in \mathbb{R}^D are far too restricted as a class of geometric objects for modeling anatomical surfaces in our main application (c.f. Section 6). The rest of this section will be devoted to generalizing the convergence rate for squared exponential kernels (9) to their reweighted counterparts (12), and more importantly, for submanifolds of the Euclidean space. The crucial ingredient is an estimate of the type (37) bounding the sup-norm of the squared power function using fill distances, tailored for restrictions of the squared exponential kernel

$$K_\epsilon(x, y) = \exp\left(-\frac{1}{2\epsilon}\|x - y\|^2\right), \quad x, y \in M \quad (40)$$

as well as the reweighted version

$$K_\epsilon^w(x, y) = \int_M w(z) \exp\left[-\frac{1}{2\epsilon}\left(\|x - z\|^2 + \|z - y\|^2\right)\right] d\text{vol}_M(z), \quad x, y \in M \quad (41)$$

where $w : M \rightarrow \mathbb{R}_{\geq 0}$ is the non-negative weight function. Note that when $w(x) \equiv 1, \forall x \in M$ the reweighted kernel (41) does not coincide with the squared exponential kernel (40), no even up to normalization, since the domain of integration is M instead of the entire \mathbb{R}^D . It is not straightforward either to naïvely enclose the compact manifold M with a compact, convex subset Ω of the ambient space and reuse Theorem 3 by extending/restricting functions to/from M to Ω , since the samples are constrained to lie on M but the convergence will be in terms of fill distances in Ω . Nevertheless, the desired bound can be established using local parametrizations of the manifold, i.e., working within each local Lipschitz coordinate chart and taking advantage of the compactness of M .

We will henceforth impose no additional assumptions, other than compactness and smoothness, on the geometry of the Riemannian manifold M . In the first step we refer to a known uniform estimate from [145, Theorem 17.21] for power functions on a compact Riemannian manifold.

Lemma 2. *Let M be a d -dimensional C^ℓ compact manifold isometrically embedded in \mathbb{R}^D (where $D > d$), and let $\Phi \in C^{2k}(M \times M)$ be any positive definite kernel function on $M \times M$ with $2k \leq \ell$. There exists a positive constant $h_0 = h_0(M) > 0$ depending only on the geometry of the manifold M such that, for any collection of n distinct points $\mathcal{X}_n = \{x_1, \dots, x_n\}$ on M with $h_{\mathcal{X}_n} \leq h_0$, the following inequality holds:*

$$\Pi_{\Phi, \mathcal{X}_n} = \sup_{x \in M} P_{\Phi, \mathcal{X}_n}(x) \leq Ch_{\mathcal{X}_n}^{2k}$$

where $C = C(k, M, \Phi) > 0$ is a positive constant depending only on the manifold M and the kernel function Φ . This of course further implies for all $h_n \leq h_0$

$$\inf_{\mathcal{X}_n \subset M, |\mathcal{X}_n|=n} \Pi_{\Phi, \mathcal{X}_n} \leq Ch_n^{2k}$$

where h_n is the minimum fill distance of n arbitrary points on Ω (c.f. (38)).

Proof. This is essentially [145, Theorem 17.21], with the only adaptation that the definition of the power function throughout [145] is the square root of the P_{Φ, \mathcal{X}_n} in our definition (34). \square

Lemma 2 suggests that the convergence of Algorithm 1 is faster than any polynomial of h_n . The dependence on h_n can be made more direct in terms of the number of samples n by the following geometric lemma.

Lemma 3. *Let M be a d -dimensional C^ℓ compact Riemannian manifold isometrically embedded in \mathbb{R}^D (where $D > d$). Denote ω_{d-1} for the surface measure of the unit sphere in \mathbb{R}^d , and $\text{Vol}(M)$ for the volume of M induced by the Riemannian metric. There exists a positive constant $N = N(M) > 0$ depending only on the manifold M such that*

$$h_n \leq \left(\frac{2^{d+1}d}{\omega_{d-1}} \text{Vol}(M)\right)^{\frac{1}{d}} \cdot n^{-\frac{1}{d}} \quad \text{for any } \mathbb{N} \ni n \geq N.$$

Proof. For any $r > 0$ and $x \in M$, we denote $B_r^D(x)$ for the (extrinsic) D -dimensional Euclidean ball centered at $x \in M$, and set $B_r(x) := B_r^D(x) \cap M$. In other words, $B_r(x)$ is a ball of radius r centered at $x \in M$ with respect to the “chordal” metric on M induced from the ambient Euclidean space \mathbb{R}^D . Define the *covering number* and the *packing number* for M with respect to the chordal metric balls by

$$\begin{aligned} \mathcal{N}(r) &:= \mathcal{N}(M, \|\cdot\|_D, r) := \min_{N \in \mathbb{N}} \left\{ M \subset \bigcup_{i=1}^n B_r(x_i) \mid x_i \in M, 1 \leq i \leq n \right\}, \\ \mathcal{P}(r) &:= \mathcal{P}(M, \|\cdot\|_D, r) := \max_{N \in \mathbb{N}} \left\{ \bigcup_{i=1}^n B_{r/2}(x_i) \subset M, B_{r/2}(x_i) \cap B_{r/2}(x_j) = \emptyset \text{ for all } 1 \leq i \neq j \leq n \mid x_i \in M, 1 \leq i \leq n \right\}. \end{aligned}$$

By the definition of fill distance and h_n (c.f. (38)), the covering number $\mathcal{N}(h_n)$ is lower bounded by n ; furthermore, by the straightforward inequality $\mathcal{P}(r) \geq \mathcal{N}(r)$ for all $r > 0$, we have

$$n < \mathcal{N}(h_n) \leq \mathcal{P}(h_n),$$

i.e. there exist a collection of n points $x_1, \dots, x_n \in M$ such that the n chordal metric balls $\{B_{h_n/2}(x_i) \mid 1 \leq i \leq n\}$ form a packing of M . Thus

$$\sum_{i=1}^n \text{Vol}(B_{h_n/2}(x_i)) \leq \text{Vol}(M) < \infty$$

where the last inequality follows from the compactness of M . The volume of each $B_{h_n/2}(x_i)$ can be expanded asymptotically for small h_n as (c.f. [67])

$$\text{Vol}(B_{h_n/2}(x)) = \frac{\omega_{d-1}}{d} \left(\frac{h_n}{2}\right)^d \left[1 + \frac{2\|B\|_x^2 - \|H\|_x^2}{8(d+2)} \left(\frac{h_n}{2}\right)^2\right] + O(h_n^{d+3}) \quad \text{as } h_n \rightarrow 0 \quad (42)$$

where ω_{d-1} is the surface measure of the unit sphere in \mathbb{R}^d , B is the second fundamental form of M , and H is the mean curvature normal. The compactness of M ensures the boundedness of all these extrinsic curvature terms. Pick n sufficiently large so that h_n is sufficiently small (again by the compactness of M) to ensure

$$\text{Vol}(B_{h_n/2}(x)) \geq \frac{\omega_{d-1}}{2d} \left(\frac{h_n}{2}\right)^d.$$

It then follows from (42) that

$$\frac{n\omega_{d-1}}{2d} \left(\frac{h_n}{2}\right)^d \leq \text{Vol}(M) \quad \Rightarrow \quad h_n \leq \left(\frac{2^{d+1}d}{\omega_{d-1}} \text{Vol}(M)\right)^{\frac{1}{d}} \cdot n^{-\frac{1}{d}}.$$

□

We are now ready to conclude that Algorithm 1 converges faster than any inverse polynomials in the number of samples with our specific choice of kernel functions, regardless of the presence of reweighting.

Theorem 4. *Let M be a d -dimensional C^∞ compact manifold isometrically embedded in \mathbb{R}^D (where $D > d$), and let $\Phi \in C^\infty(M \times M)$ be any positive definite kernel function on M . For any $k \in \mathbb{N}$, there exist positive constants $N = N(M) > 0$ and $C_k = C_k(M, \Phi) > 0$ such that*

$$\sigma_n \leq C_k n^{-\frac{k}{d}} \quad \text{for all } n \geq N.$$

In words, Algorithm 1 converges at rate $O(n^{-\frac{k}{d}})$ for all $k \in \mathbb{N}$.

Proof. Use Lemma 2, Lemma 3 and the regularity of the kernel function Φ . □

Though it is natural to conjecture that exponential rate of convergence holds at least for the Euclidean radial basis kernel (40), Theorem 4 is about as far as we can get with our current techniques, unless we impose additional assumptions on the regularity of the manifolds of interest. It is tempting to proceed directly as in [145, Theorem 17.21] by working locally on coordinate charts and citing the exponential convergence result for radial basis kernels in [145, Theorem 11.22]; unfortunately, even though kernel K_ϵ is of radial basis type in the ambient space \mathbb{R}^D , it is generally no longer of radial basis type in local coordinate charts, unless one imposes additional restrictive assumptions on the growth of the derivatives of local parametrization maps (e.g. all coordinate maps are affine). We will not pursue the theoretical aspects of these additional assumptions in this paper.

Remark 5. *The asymptotic optimality of the rate established in Theorem 4 for Gaussian process landmarking follows from Theorem 2. In other words, the Gaussian process landmarking algorithm leads to a rate of decay of the ∞ -norm of conditional covariances that is at least as fast as any other landmarking algorithms, including random or uniform sampling on the manifold. In our application of comparative biology that motivated this paper, it is more important that Gaussian process landmarking is capable of identifying biologically meaningful and operationally homologous points across the anatomical surfaces even when the number of landmarks is small ($n \ll \infty$); see e.g. Figure 6 in Section 6.1. A more thorough theory explaining this advantageous aspect of Gaussian process landmarking will be left for future work.*

6 Application in Automated Geometric Morphometrics

This section is divided into three parts. Section 6.1 compares Gaussian process landmarks generated from Algorithm 1 with “ground truth” landmarks manually picked by comparative biologists on a real dataset of anatomical surfaces, demonstrating comparable levels of coverage of biologically significant features. The results presented in this section provide quantitative evidence that Gaussian process landmarks are capable of capturing geometric features encoding important information for comparative biologists on individual anatomical surfaces. Section 6.2 adapts the image feature matching algorithm of [81] for the registration of pairs of anatomical surface via matching Gaussian process landmarks computed on each individual surface. We compare the resulting shape correspondence maps with a baseline obtained using previously developed *continuous Procrustes analysis* in [2, 19]; the results suggest that, though Gaussian process landmarks are generated on each individual shape separately, they implicitly encode operationally homologous features that can be compared and contrasted across shapes, and such pairwise comparison results are comparable with those obtained from standard Procrustes shape analysis based on “ground truth” observer landmarks. The pairwise shape distances induced from matching landmarks are turned into ordination plots (two-dimensional embeddings of distance matrices, commonly employed for visualizing the “morphospace” characterizing shape variances) in Section 6.3; it turns out that Gaussian process landmarks lead to a favorable ordination, which is in better agreement with observations made by comparative biologists and paleontologists in existing literature.

6.1 Unsupervised Landmarking on Individual Anatomical Surfaces

Gaussian process landmarks are generated on each anatomical surface individually, regardless of the size of the shape collection; the landmarks manually selected by human experts (observers), however, may well depend on the information gradually exposed to the human expert as he/she moves through a collection of surfaces. It is thus surprising that the individually generated, “local” Gaussian process landmarks bear an unignorable amount of similarity with the observer landmarks selected with certain extent of collection-wise or “global” knowledge, as we have already illustrated in Figure 2 through an example fossil molar. This subsection is devoted to a more thorough and quantitative comparison between Gaussian process landmarks and “ground truth” observer landmarks placed by human experts.

We begin by collecting in Figure 5 examples applying the Gaussian Process Landmarking algorithm to other types anatomical surfaces than molars, namely, a subset of the astragalus and calcaneus bones of tarsiers first published in [20]. Though observer landmarks are not available for this dataset and thus we can not directly compare automatically generated landmarks with manually placed ones, it can be recognized from Figure 5 that the algorithm is capable of consistently capturing both geometric features (“Type 3 landmarks” [117]) and semilandmarks (delineating ridges and grooves), which is consistent with the results for the molar dataset.

To quantitatively validate the similarity between Gaussian process landmarks and observer landmarks, we calculate, on each anatomical surface, the median geodesic distance from an observer landmark to its closest Gaussian process landmark. This median geodesic distance can obviously be calculated for any other type of landmarks in place of the Gaussian process landmarks; we shall refer to it as the *median observer-to-automatic landmark distance*, for the sake of simplicity. Since the number of automatic landmarks is typically difficult to fix *a priori*, we compute the median observer-to-automatic landmark distances for a varying number of automatic landmarks, obtaining a curve that encodes the rate with which the median observer-to-automatic landmark distances decay to zero as the number of automatic landmarks increases. Comparing curves obtained from different automatic landmark generation methods then provides us with a way to compare how closely each type of automation “mimics” the observer landmarks. When we perform such curve comparisons for a large collection of surfaces in a dataset, one can in principle construct statistics (e.g. “mean” or “standard deviation” in the “space of curves”) along the lines of *Functional Data Analysis* (FDA, see e.g. [112, 111] and the references therein), but we will have to defer such a statistically systematic treatment to future work.

Using this strategy, we compare Gaussian process landmarks with landmarks obtained from *Geodesic Farthest Point Sampling* (GFPS) [52, 91], a popular downsampling technique in automated geometric morphometrics, on a dataset of 116 second mandibular molars of prosimian primates and closely related non-primates first published in [19]. GFPS is known to produce approximately uniformly distributed points on surfaces, with respect to the canonical surface volume measure. In our numerical experiments in this subsection, we choose the first point in GFPS to be the same as the first point obtained by Gaussian process landmarking, to eliminate the effects of random initialization. As a baseline, we also calculate the median observer-to-automatic landmark distances for completely randomly picked vertices on the triangular meshes in this dataset. The results are presented in Figure 6, in which each curve is obtained

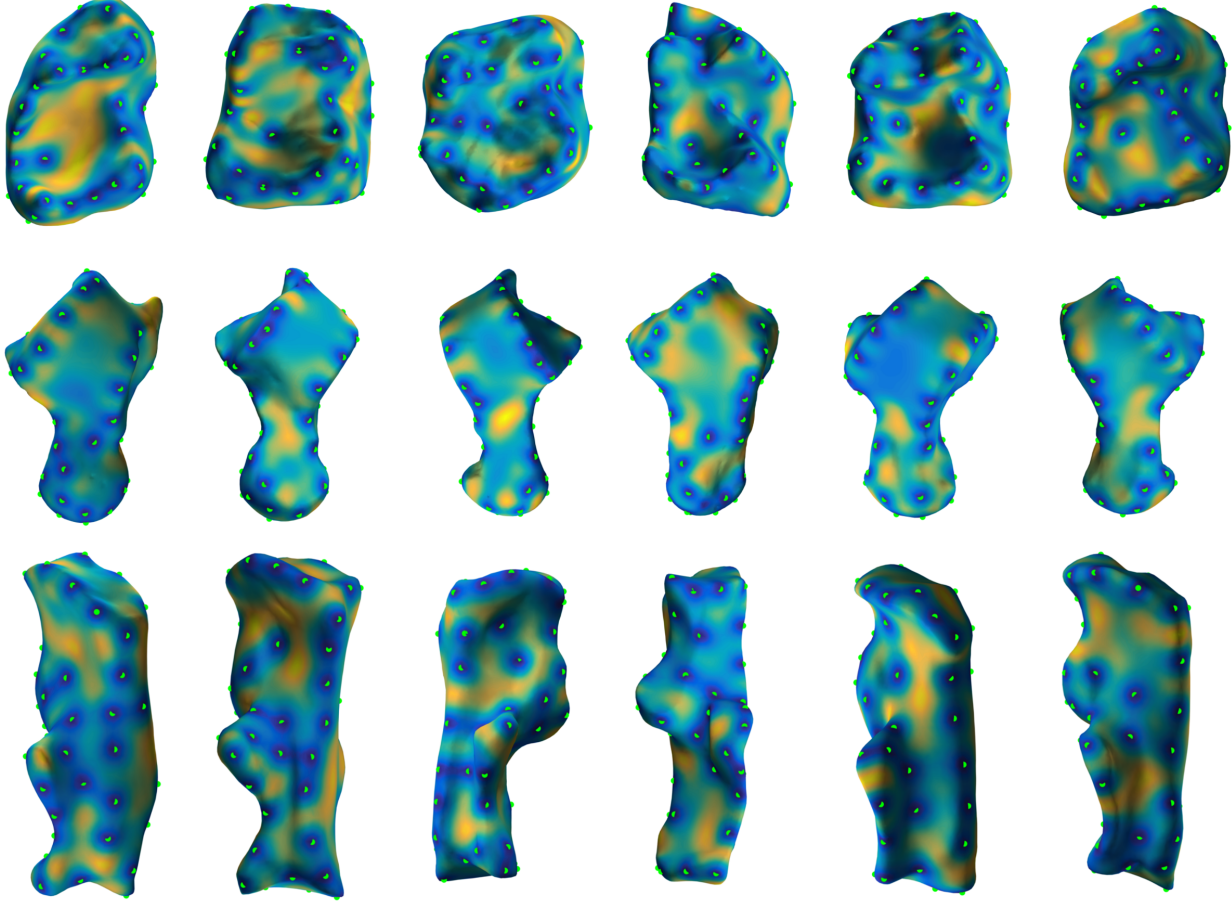


Figure 5: Gaussian process landmarks on several different types of anatomical surfaces. All triangular meshes are acquired from μ CT scans. **Top Row:** Six second mandibular molars of prosimian primates and non-primate close relatives, from a dataset of 116 molars first published in [19]. **Middle Row:** Six astragalus bones of tarsiers from a dataset of 40 astragali first published in [20]. **Bottom Row:** Six calcaneus bones of tarsiers from a dataset of 40 calcanei first published in [20]. On all three types of anatomical surfaces, Gaussian process landmarks tend to play the roles of both landmarks and semilandmarks (c.f. [151, §2]): the curvature-reweighted kernel promotes automatically selecting sharp peaks or saddle points on the anatomical surface; after most of the prominent geometric features—normally recognized as Type 2 landmarks [151]—are captured, the uncertainty-based criterion encourages the identification of semilandmark-type points along ridges and grooves.

by averaging individual curves over the entire shape collection; confidence intervals of one standard deviation are also plotted in shades of transparency. Figure 6 suggests that Gaussian process landmarks consistently outperforms GFPS landmarks and the random baseline in terms of coverage of observer landmarks.

6.2 Pairwise Surface Registration by Matching Gaussian Process Landmarks

We demonstrate in this subsection the benefit of using Gaussian process landmarks for establishing correspondences between pairs of surfaces. In particular, although Gaussian process landmarks are obtained independently on each surface, they turn out to encode geometrically significant features — shared more often among similar or related shapes — that are recognized as “operational homologous” [20] loci by comparative biologists. Statistical analysis also suggest that these correspondence maps reach comparable explanatory power to observer landmarks placed by human experts, in terms of induced shape distances. The comparison between the morphospaces characterized by these shape distances is deferred to Section 6.3.

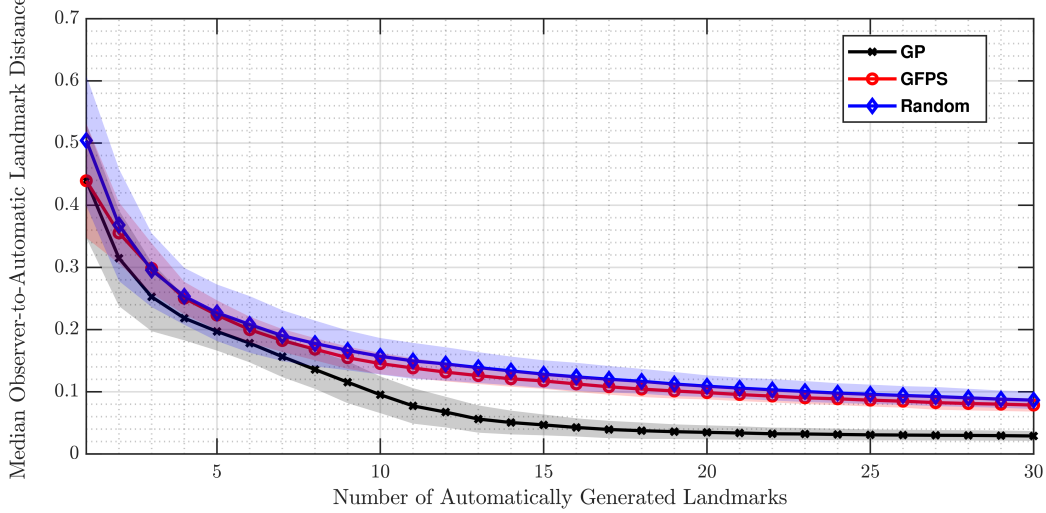


Figure 6: Median geodesic distance from an observer landmark to its nearest automatically generated landmark, with respect to different numbers of automatic landmarks, on a collection of 116 second mandibular molars of prosimian primates and closely related non-primates (see [19] for a more detailed description of this dataset and the observer landmark acquisition). Each point on any of the three solid curves is obtained by averaging the 116 median observer-to-automatic landmark distances over the entire dataset, and the transparent bands represent confidence intervals of one standard deviation. The three types of automatic landmarks are Gaussian process landmarks (GP), geodesic farthest point sampling landmarks (GFPS), and random landmarks uniformly selected from the vertices of each triangular mesh. The random landmarks are only used as a baseline in this experiment.

6.2.1 Experimental Setup and Methodology

Bounded Distortion Gaussian Process Landmark Matching. Let S_1, S_2 be two-dimensional disk-type surfaces (conformally equivalent to planar disks by the Uniformization Theorem; see e.g. [2, 79, 80]) and let $\xi_1^{(1)}, \dots, \xi_{L_1}^{(1)} \in S_1$ and $\xi_1^{(2)}, \dots, \xi_{L_2}^{(2)} \in S_2$ be two sets of Gaussian process landmarks computed using Algorithm 1 on S_1 and S_2 , respectively. Note that the algorithm we present in this subsection works equally well for $L_1 \neq L_2$, though we choose $L_1 = L_2 = 40$ throughout this paper to simplify the discussion. Adopting the approach suggested in [81] for feature-based image matching, we devise the following two-step approach for establishing geometrically-consistent matchings between the two sets of Gaussian process landmarks:

- (1) *Parametrization:* For each surface S_j ($j = 1, 2$) we follow [132, 72] to compute an as-isometric-as-possible (AIAP) two-dimensional parametrization, which is a diffeomorphism $\Phi_j : S_j \rightarrow \Omega_j \subset \mathbb{R}^2$ from S_j to a connected planar domain Ω_j minimizing the (discretization of the) *isometric distortion energy*

$$F(\phi) := \int_{S_j} \left(|\nabla \phi(x)|^2 + |\nabla \phi^{-1}(x)|^2 \right) d\text{vol}_M(x). \quad (43)$$

Each landmark $\xi_\ell^{(j)}$ is mapped to a unique corresponding point $\zeta_\ell^{(j)} = \Phi_j(\xi_\ell^{(j)}) \in \Omega_j \subset \mathbb{R}^2$, where

$$\Phi_j := \underset{\phi: S_j \rightarrow \mathbb{R}^2}{\text{argmin}} F(\phi).$$

- (2) *Bounded Distortion Matching:* Following [81], we search within the set of planar diffeomorphisms between Ω_1 and Ω_2 with *conformal distortion* [78] bounded by a pre-fixed constant $K \geq 1$. This algorithm strives to find a maximal subset of geometrically-consistent correspondences within an initial set of candidate matches. In the extreme case of $K = 1$, the search is constrained within the set of strictly angle-preserving (conformal) maps for the continuous isometric distortion energy and the set of planar rigid transformations for the discretized isometric distortion energy; we select $K = 1.5$ in this experiment to slightly enlarge the search space of candidate maps.

As input to this matching algorithm, for each Gaussian process landmark $\zeta_\ell^{(1)}$ on S_1 , we choose $T \geq 2$ Gaussian process landmarks $\zeta_{\ell \rightarrow 1}^{(2)}, \dots, \zeta_{\ell \rightarrow T}^{(2)}$ as initial putative candidate matches from the Gaussian process landmarks

$\{\zeta_j^{(2)} \mid 1 \leq j \leq L_2\}$ on S_2 ; the algorithm then searches for the bounded distortion map $\Psi : \Omega_1 \rightarrow \Omega_2$ that minimizes the mismatch count

$$\sum_{\ell=1}^{L_1} \sum_{k=1}^T \left\| \Psi(\zeta_\ell^{(1)}) - \zeta_{\ell \rightarrow k}^{(2)} \right\|^0, \quad (44)$$

where, following the notations of [81], $\|\cdot\|^0$ denotes the mixed $(2, 0)$ -norm defined as

$$\left\| \Psi(\zeta_\ell^{(1)}) - \zeta_{\ell \rightarrow k}^{(2)} \right\|^0 = \begin{cases} 1 & \text{if } \Psi(\zeta_\ell^{(1)}) \neq \zeta_{\ell \rightarrow k}^{(2)}, \\ 0 & \text{otherwise.} \end{cases}$$

The initial candidate matches in our experiments are generated by comparing the *Wave Kernel Signature* (WKS) [7] of the Gaussian process landmarks — the T Gaussian process landmarks on S_2 with most similar WKS's (measured in Euclidean distances) with that of each $\zeta_\ell^{(1)} \in S_1$ are selected as $\{\zeta_{\ell \rightarrow t}^{(2)} \mid 1 \leq t \leq T\}$. Ideally, “incorrect” initial matches potentially leading to large conformal distortions will be filtered out by minimizing (44) under the bounded conformal distortion constraint. Our implementation uses $T = 2$ which turned out to be an empirically satisfactory choice.

The pairwise registration algorithm outputs a subset of $1 \leq L \leq \min\{L_1, L_2\}$ one-to-one correspondences $\tilde{\zeta}_\ell^{(1)} \leftrightarrow \tilde{\zeta}_\ell^{(2)}$, $\ell = 1, \dots, L$, from the initial $L_1 T$ candidate Gaussian process landmark matches; the number of matched landmarks, L , is automatically determined by the final bounded distortion map and could be vary between different pairs. A final step in this algorithm pipeline “interpolates” the L pairs of matched Gaussian process landmarks to obtain a diffeomorphism between the surfaces S_1 and S_2 . For this purpose, we use the technique developed in [132, 72] which computes a map $\tilde{\Psi} : \Omega_1 \rightarrow \Omega_2$ that minimizes the isometric distortion energy (43) subject to the L linear equality constraints $\tilde{\Psi}(\tilde{\zeta}_\ell^{(1)}) = \tilde{\zeta}_\ell^{(2)}$ ($1 \leq \ell \leq L$) representing the “sparse” correspondences between Gaussian process landmarks. The composition $f_{12} = \Phi_2^{-1} \circ \tilde{\Psi} \circ \Phi_1$ finally produces the desired map $f : S_1 \rightarrow S_2$ that approximately minimizes the mismatch count (44). This last interpolation step is indispensable for the purpose of interpretability (producing full-surface registrations for visual comparisons) as well as evaluation (inducing shape Procrustes distances for ordination, see Section 6.3). Figure 7 outlines the complete workflow of landmark matching and surface registration for a pair of molars surfaces from [19]; a few examples are shown in Figure 8.

Evaluation Metrics and the Baseline. We demonstrate the rich taxonomic information captured by the maps output from the proposed bounded distortion Gaussian process landmark matching (GP-BD) algorithm, by comparing the shape *Procrustes distances* induced by maps computed from GP-BD with those obtained by the same feature matching methodology but alternative choices of landmarking schemes. For any inter-surface map $f : S_1 \rightarrow S_2$, we define the *Procrustes distance induced by f* as

$$d_P(f) = \left(\min_{R \in \mathbb{E}_3} \int_{S_1} \|f(x) - R(x)\|^2 \, d\text{vol}_{S_1}(x) \right)^{\frac{1}{2}}, \quad (45)$$

where \mathbb{E}_3 stands for the rigid motion group in \mathbb{R}^3 . The distance $d_P(f)$ measures the spatial registration error induced by the map f between the two surfaces. To ensure that the Procrustes distances induced by the various methods listed in Table 1 is comparable, we normalize each surface to have unit surface area. When the map f is the continuous Procrustes map produced from the algorithm presented in [2], d_P gives exactly the *continuous Procrustes distance* between S_1 and S_2 .

The alternatives considered in this section include two other different types of Gaussian process landmarks (GP_{nW}-BD and GP_{Euc}-BD) with alternative kernel functions (different from (18)), two different strategies of utilizing the “ground truth” user-placed observer landmarks (GT-BD and GT²-BD), as well as the baseline *continuous Procrustes maps* (CPM) reported in [2, 19]; Table 1 provides a summary of these variants. Specifically, GP_{Euc}-BD and GP_{nW}-BD are based on Gaussian processes with the standard squared exponential kernel (9) and the trivially weighted kernel (10) (or equivalently, setting $w \equiv 1$ in (12)), respectively. GT-BD simply replaces the GP landmarks with “ground truth” (GT) landmarks, which then follows through with candidate selection via WKS and BD-filtering; GT²-BD also takes ground truth landmarks as inputs, but skips the candidate selection by setting the ground truth correspondences between observer landmarks as candidate matches, though BD-filtering still applies and prunes out potential “geometrically incompatible” correspondences leading to large conformal distortions. A detailed description of observer landmark acquisition can be found in [19].

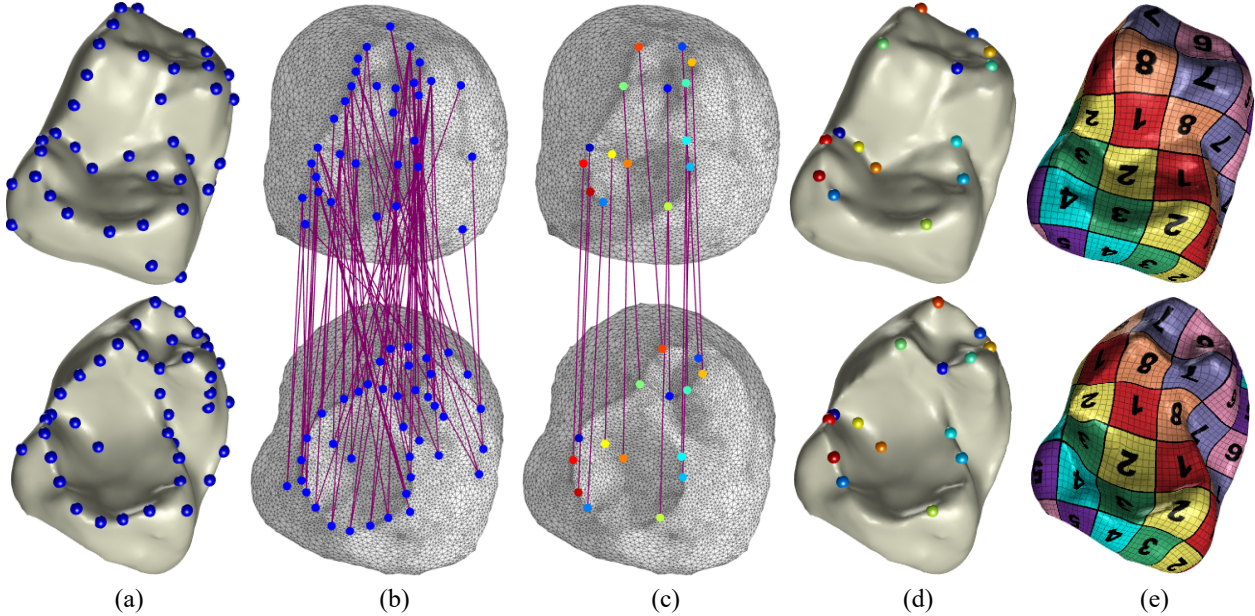


Figure 7: The outline of our approach for landmark matching and surface registration. (a) Gaussian process landmarks computed using Algorithm 1 on two surfaces; (b) planar parameterizations of the surfaces that minimize (43), overlaid with putative landmark matches (indicated by purple lines); (c) Bounded-Distortion correspondences: a subset of geometrically-consistent matches computed by approximately minimizing (44); (d) Paris of corresponding Gaussian process landmarks found by bounded distortion matching, illustrated by spheres with matching colors; (e) Texture-map visualization of an inter-surface map interpolating the landmark correspondences depicted in (d).

The shape distances will be compared in several different ways. We will first compare cumulative distributions of the pairwise shape distance values, followed by two statistical tests addressing (i) the correlation between each automatic shape distance and the observer-determined landmarks Procrustes distance (ODLP), and (ii) the capability of each shape distance at distinguishing taxonomic groups. A qualitative but more intuitive comparison of the *morphospaces* [90] characterized by these shape distances will be deferred to Section 6.3, in the form of ordination plots (two dimensional embedding of the shape distance matrices as visual representations for shape variances across species groups). The discussion in Section 6.3 is however oriented slightly more towards comparative biologists.

6.2.2 Comparison Results

We compared the pairwise surface registration methods listed in Table 1 on a dataset consisting of 116 triangular meshes representing surfaces of the second mandibular molars of prosimian primates and closely related non-primates [19]. We computed correspondences between each pair of surfaces within this dataset, totaling in over 13,000 inter-surface registrations.

Figure 8 shows example pairs of surfaces, visualizing inter-surface maps induced by GP-BD correspondences as well as the baseline CPM maps. These examples illustrate typical differences between maps computed from GP-BD and CPM along with their Procrustes distances; GP-BD maps often offer an improvement over CPM in terms of both visual quality and their ability to relate biologically meaningful and operationally homologous regions.

Comparing Cumulative Distributions of Distance Values. We first provide a crude comparison across the various methods listed in Table 1. Figure 9 plots the cumulative distributions of Procrustes distances induced by each type of pairwise registration method in Table 1, which serves as a direct comparison of the proportions of pairwise inter-surface correspondences for which the Procrustes distance d_P (45) is below a given threshold. The figure further includes a curve for the Observer-Determined Landmarks Procrustes (ODLP) distances, computed using the standard Procrustes analysis between sets of corresponding landmarks manually placed by human experts [19]. Recall from Section 6.2.1 that the surface areas are normalized so as to ensure that Procrustes distances induced by different shape correspondences are comparable.

Abbreviation	Description of the pairwise surface registration method
GP-BD	Bounded Distortion (BD) filtering for Gaussian process (GP) landmarks computed with Algorithm 1
GP _{Euc} -BD	Bounded Distortion (BD) filtering for Gaussian process (GP) landmarks computed with the standard Euclidean heat kernel (9)
GP _{nW} -BD	Bounded Distortion (BD) filtering for Gaussian process (GP) landmarks computed with a non-weighted kernel (10)
GT-BD	Bounded Distortion (BD) filtering for ground truth (GT), observer-placed landmarks
GT ² -BD	Bounded Distortion (BD) filtering for ground truth (GT), observer-placed landmarks, also using the ground truth correspondences as candidate initial matches
CPM	Continuous Procrustes inter-surface Maps (CPM) computed using the method of [19, 2]

Table 1: The pairwise surface registration methods compared in Section 6.2 and Section 6.3.

Noticeably, the cumulative distribution of GP-BD distances most closely resemble that of GT-BD, obtained by replacing the Gaussian process landmarks with the ground-truth observer landmarks (but otherwise using exactly the same algorithm involving WKS and BD-filtering). Also, GP-BD outperforms GP_{nW}-BD (Gaussian process with a trivially weighted kernel) and GP_{Euc}-BD (Gaussian process with the standard Euclidean heat kernel). This comparison suggests that the Gaussian process landmarks computed with Algorithm 1 provide a good proxy for geometrically significant features needed to determine meaningful correspondences between surfaces.

Expectedly, GP-BD falls short compared to distances that rely on both the ground-truth observer landmarks and their true correspondences (GT²-BD and ODLP). Comparing GP-BD to the baseline continuous Procrustes maps (CPM) in terms of distance distributions is equivocal as the two curves in Figure 9 cross each other when the Procrustes distance threshold is about 0.15. Nonetheless, comparing GP-BD to CPM indicates that the former produces more pairwise correspondences with shape distances less than 0.1 (at which the vertical gap between the two curves reaches its maximum). This, along with the correlation reported in [45] between smaller cP distances and better morphometric interpretability of the associated maps, implies that Gaussian process landmarks potentially lead to more stable and interpretable comparative biological analysis if combined with other globally transitive geometric morphometric methods. Further validation will have to be left for future exploration.

Statistical Tests Comparing the Distance Matrices. We now provide a more thorough comparison — using non-parametric statistical tests — for the shape distance matrices induced by the various methods listed in Table 1. Treating the OPLD (Observer-Determined Landmarks Procrustes distance) matrix as a proxy for the “ground truth” accepted among geometric morphometrists (c.f. [19]), we first compare the correlation between each automatically computed shape distance matrix with ODLP using the *Mantel correlation test* [86]; the explanatory power of the shape distances (in terms of the ability to distinguish taxonomic groups) are then compared using a variant of the multivariate analysis of variance (MANOVA) for distance matrices.

Due to the dependence of entries in a distance matrix (e.g. constrained by the triangular inequality), assessments of correlation between distance matrices, or between a distance matrix and a (continuous or categorical) variable, often involves repeatedly permuting the rows and columns of the distance matrix. In fact, permutation test (or *randomization test*) has become an increasingly common statistical tool in the nonparametric setting; see e.g. [104, 99, 53] and the references therein. Table 2 demonstrates the results of Mantel correlation analysis [86] between the distance matrices computed in this paper against the ODLP distance matrix. GT-BD and GT²-BD correlate best with ODLP, which is as expected since they both rely directly on the same set of observer-determined landmarks used for computing the ODLP distances; their high correlation with ODLP justifies the use of bounded distortion maps for capturing biologically meaningful and corresponding geometric features. GP-BD outperforms CPM, which is consistent with our observation in Figure 9 that a majority (over 80%) of the distance values computed from GP-BD is more similar in distribution to the distances computed with ground truth landmarks. The advantageously higher correlation of GP-BD over GP_{Euc} and GP_{nW} illustrates the importance of reweighting in the kernel construction.

We also perform Permutational Multivariate Analysis of Variance (PERMANOVA) [4] for the distance matrices computed in this paper, with the taxonomic groups shown in the ordination plots (Figure 10, see detailed explanations in Section 6.3) as the treatment effects. The result is presented in Table 3. The purpose of this test is to quantitatively compare the power of differentiating taxonomic groups for these distance matrices. The pseudo *F*-statistics in

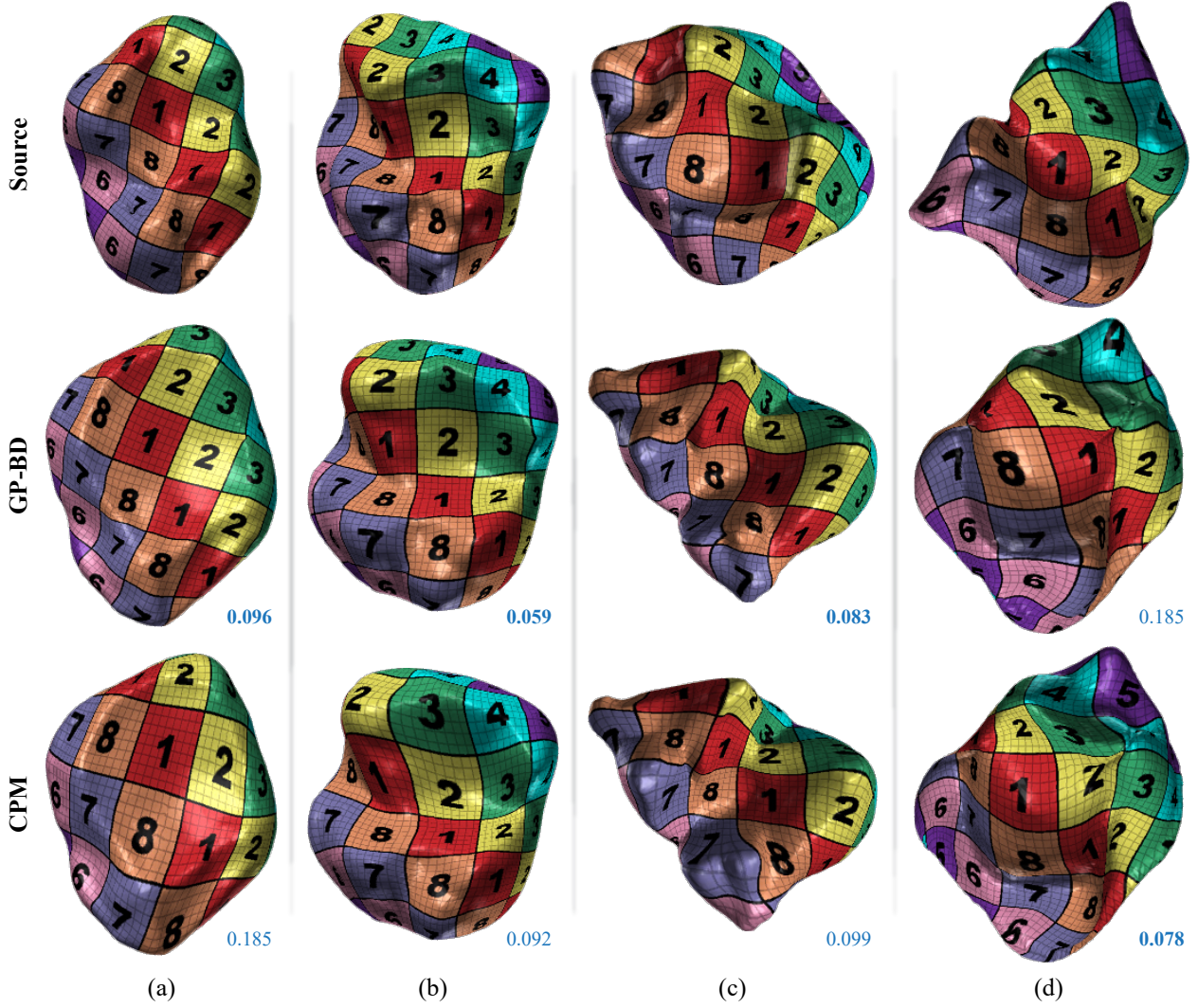


Figure 8: Inter-surface maps and induced Procrustes distances: texture overlaid on the Source surface (top row) is mapped by $f : S_1 \rightarrow S_2$ so as to visualize correspondence. The second row (GP-BD) shows maps induced by correspondences established between Gaussian process landmarks computed with Algorithm 1. The bottom row (CPM) compares the baseline continuous Procrustes maps. GP-BD outperforms CPM in examples (a)-(c), wherein the map it induces establishes a better correspondence between morphological features of the surfaces; example (d) shows a case in which GP-BD is outperformed by CPM. The inset values are the the Procrustes distance d_p associated with each map.

PERMANOVA is a properly normalized ratio between among-group and within-group sum of squared distances. The statistical significance is then calculated from the fraction—among sufficiently many shuffles of the rows and columns of the distance matrix—of the permutation instances that produce a higher pseudo F -ratio. While all distance matrices demonstrate statistically significant pseudo F -ratios in this test, the GT-BD distance matrix leads the board of pseudo F -ratios, indicating its superior ability of separating taxonomic groups; the GP-BD distance matrix and its two variants consistently outperform CPM in terms of pseudo F -ratios, verifying again the improved quality of pairwise anatomical surface registrations as well as the induced shape Procrustes distances.

6.3 Ordination and Comparative Biological Interpretation for Shape Collections

This subsection provides a qualitative but visually more straightforward way to compare the shape distance matrices obtained from the various pairwise registration methods in Table 1 on a collection of shapes. The results presented here suggests that a proper mechanism matching Gaussian process landmarks can potentially capture more morphometrical

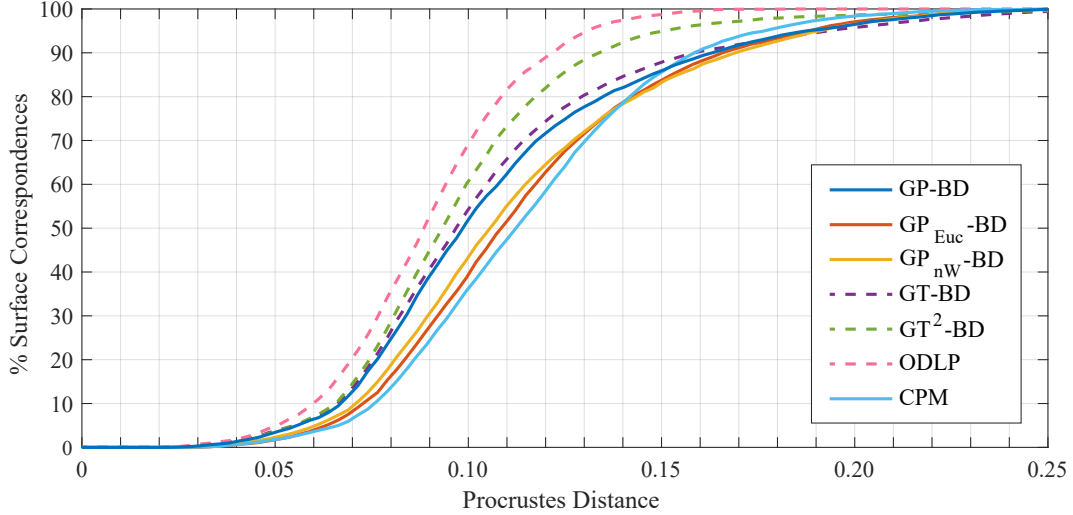


Figure 9: Comparing GP-BD to the alternative methods listed in Table 1. Each curve represents the proportion of correspondences, among a collection of 116 surfaces, for which the Procrustes distance d_P falls below a given threshold. The cumulative distribution of GP-BD distances most closely resembles that of GT-BD which utilizes the ground truth observer landmarks. It falls short of GT²-BD and the Observer-Determined Landmarks Procrustes (ODLP), both of which rely additionally on the “ground truth” correspondences between observer landmarks. In terms of producing more relatively smaller distances between the shape pairs (which is favorable by the correlation between smaller distances and enhanced morphometric interpretability reported in [45]; also suggested by the cumulative distribution curves of ODLP, GT²-BD, and GT-DB), GP-BD outperforms the baseline continuous Procrustes maps (CPM), as well as variants of Gaussian process landmarks with alternative kernel constructions, GP_{nW}-BD (Gaussian process landmarks with a non-weighted kernel) and GP_{Euc}-BD (Gaussian process landmarks with a standard Euclidean heat kernel).

	GT-BD	GT ² -BD	CPM	GP-BD	GP _{Euc} -BD	GP _{nW} -BD
corr. coeff.	0.7042	0.7563	0.6647	0.6870	0.6135	0.6257
<i>P</i> value	**	**	**	**	**	**

Significance codes: ** $P < 0.01$.

Table 2: Results of Mantel correlation analysis for the various distances computed in this paper versus ODLP distances. The high correlation of GT-BD and GT²-BD versus ODLP is not surprising due to their direct dependence on the observer-determined landmarks. The distance computed from GP-BD has higher correlation with ODLP than the other distances, which is consistent with the CDF plot Figure 9 and the ordination plots in Figure 10. We set the number of permutations to 9999 since it is recommended in [4] that at least 5000 permutations should be done for tests with an α -level of 0.01.

information faithfully in the induced shape distances, thus providing better characterizations of the shape variation across species groups.

Ordination and Taxonomic Classification. Comparative biologists, ecologists, and other natural and social scientists frequently rely on *ordination* or *gradient analysis* to summarize and emphasize patterns in multivariate datasets [28, 29, 4]. The equivalent but more familiar term for statisticians and applied mathematicians is *dimension reduction*. Generally speaking, it is assumed or hypothesized that groups that are distantly related or have different ecologies will display some physical differences related to these variables, but it is difficult to know which physical traits will be most affected, or whether certain traits are independent of each other. Ordination methods such as *Principal Components Analysis* (PCA), *Multi-Dimensional Scaling* (MDS), and *Correspondence Analysis* (CA) reveal the nature of those physical differences by summarizing multivariate datasets in lower dimensional graphical form.

In Figure 10 we visualize ordinations induced from four different distance matrices using classical multi-dimensional scaling (MDS). The dataset consists of 116 second mandibular molars of prosimian primates and non-primate close relatives, first published in [19]. The distances include the continuous Procrustes distance [2] and three bounded distortion map based distances with different matching criteria. In each ordination MDS plot, points corresponding to the same species group are enclosed in a polygonal, and the color pattern of the polygons indicates shape similarity among

	ODLP	GT-BD	GT ² -BD	CPM	GP-BD	GP _{Euc} -BD	GPnW-BD
pseudo <i>F</i> -ratio	12.264	16.6999	13.9038	9.42259	16.2604	11.1461	12.9873
<i>P</i> value	**	**	**	**	**	**	**

Significance codes: ** $P < 0.01$.

Table 3: PERMANOVA test results for various distance matrices computed in this paper for a collection of 116 second mandibular molars of prosimian primates and non-primate close relatives. The number of group is 30, equaling to the number of polygonal regions in the ordination plot in Figure 10. The first column refers to observer-determined landmarks Procrustes (ODLP) distances calculated in [19] as a baseline. All distance matrices are shown to be statistically significant in terms of their powers of separating species groups; the significant of GP-BD is comparable to that of GT-BD which has the highest pseudo *F*-ratio over all distances matrices considered in this paper. The number of permutations is set to 9999 for the same reason as in Table 2.

generic specimens across species groups, based on visual inspection and traditional comparative analyses. Similar ordination plots have been used for comparing different algorithms designed for automatically quantifying the geometric similarity of anatomical surfaces; see e.g. [20, 141, 45]. This type of plots can also be considered as visualizations of *morphospaces* in evolutionary and developmental biology [90].

An important criterion for good ordination is the extent to which specimens belonging to the same species group cluster near each other, and specimens from different species groups are separated from each other. A popular summary statistic is to measure the ratio between within-group distances and among-group distances, which we quantitatively calculate and present in Table 3. Nevertheless, it is already evident from qualitatively inspecting Figure 10 that bounded distortion maps (Figure 10a, Figure 10b, Figure 10d) in general better distinguish species groups than continuous Procrustes maps (Figure 10c). Considering taxonomic group membership and previous interpretations regarding shape affinities of different taxa, the ordination induced from GP-BD distances (Figure 10a) is visually most appealing. We explain some compelling examples in detail, referencing previous observations by biologists and paleontologists.

- (i) Figure 10a has a relatively low within/between-group distance ratio (see Table 3 for more details), with remarkable distinctiveness of the Indriidae, *Tupaia*, and *Cynocephalus* groups from the other groups, which is a faithful reflection of the shape dissimilarity based on visual inspections;
- (ii) Among all different ordinations presented in Figure 10, Figure 10a best separates out fossil (the brown-colored groups — Plesiadapoidea, *Plesiolestes*, *Purgatorius*, *Leptacodon*, and *Altanius*) and living non-primates (the yellow-colored groups — *Tupaia* and *Ptilocercus* (Scandentia or “treeshrews”) and *Cynocephalus* (Dermoptera)) from strepsirrhine primates and most early fossil primates (light and dark groups of lemurs — *Eulemur*, *Lemur*, *Varecia*, *Cheirogaleus*, *Hapalemur*, *Prolemur*, and *Cheirogaleidae*; light and dark green groups of Lorisidae — *Loris*, *Galago*, *Arctocebus*, *Nycticebus*, and *Perodicticus*; the red group of the extinct adapiforms and omomyiforms — *Adapis*, *Cantius*, and *Donrussellia*);
- (iii) The thought-provoking patterns of overlapping reflected in Figure 10a are in accordance with views established in existing comparative biological literature. For instance, *Tarsius* (a haplorhine primate) and plesiadapoid non-primates overlap, reflecting the idea by previous authors that they might be united in a common group called “Plesiotarsiiformes” [47, 48]. As another example, *Teilhardina*, *Donrussellia*, and *Cantius* all overlap, reflecting the fact that all of them represent very primitive members of primates: *Donrussellia* was originally thought to be a new species of *Teilhardina* [118]; *Cantius* was originally thought to be an omomyiform like *Teilhardina* instead of an adapiform [129], and [50] observed additional features of the premolar teeth uniquely relating *Cantius torresi* to *Teilhardina*. Though *Cantius* is now rerecognised as an adapiform, the wide separation between it and the other sampled adapiform (*Adapis*) also matches previous qualitative discussions and analyses of independent datasets. In particular, the fact that *Adapis* overlaps *Lemur*, *Eulemur*, and *Lepilemur* is reminiscent of arguments by [49] that *Adapis* has special affinities to the living strepsirrhines to the exclusion of other adapiforms, as well as that *Lepilemur* belongs to a group called “Megaladapidae” in part because of the claim that some members of the group have teeth extremely similar to those of *Adapis* ([124]). Analysis of other skeletal regions such as the ankle bones [125] also link *Adapis* more closely to living lemurs than to other adapiforms. Finally, the overlap of *Eosimias* with treeshrews matches the suggestion by [51] that this taxon, otherwise thought of as an anthropoid, is in fact treeshrew-like in its dentition. Again analyses of ankle bones return a similar pattern; see e.g. [149, 21].

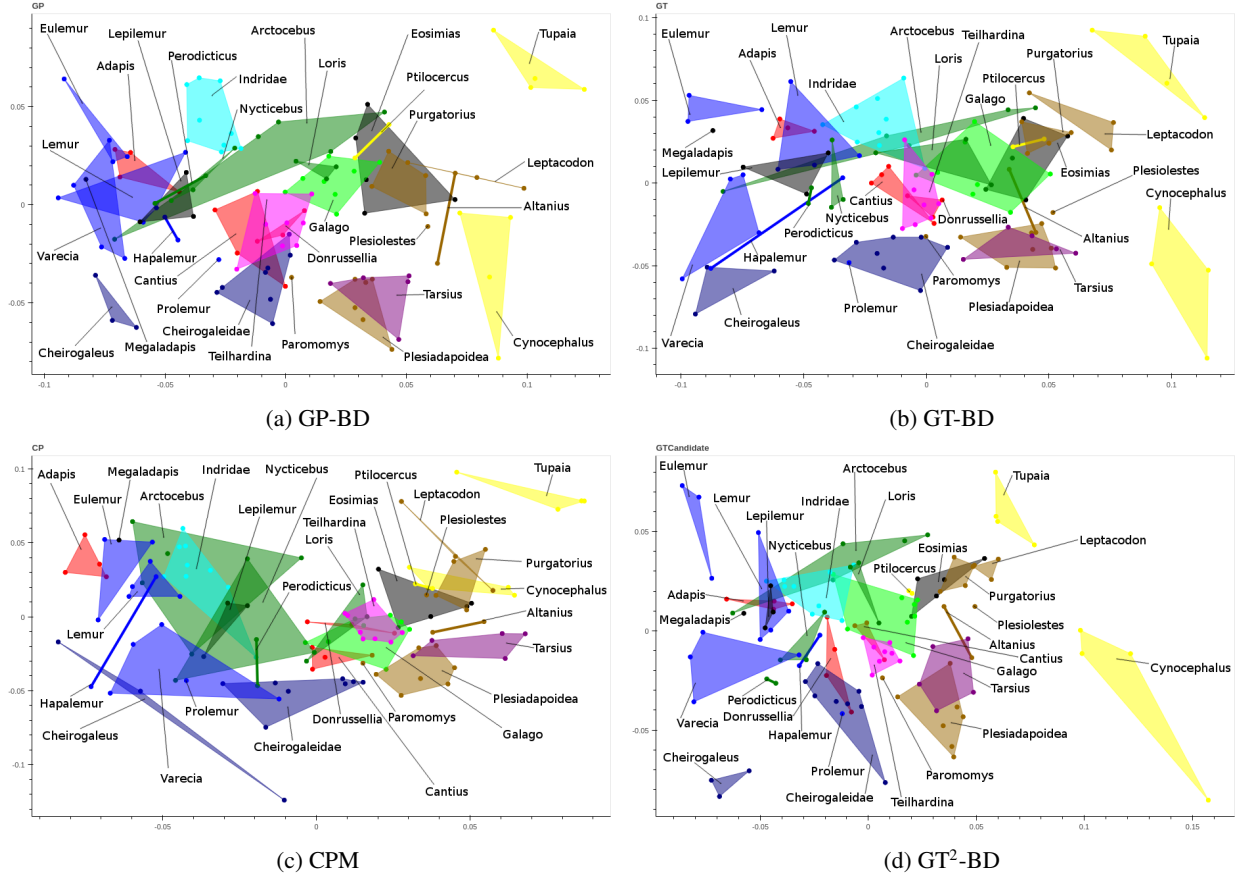


Figure 10: Multi-Dimensional Scaling (MDS) plots visualizing shape similarities characterized by four alternative distance matrices for a collection of 116 second mandibular molars of prosimian primates and non-primate close relatives. The distances investigated here include (a) Procrustes distance induced by GP-BD maps that match as many pairs of Gaussian process landmarks as possible within distortion bound $K = 1.5$; (b) Procrustes distance induced by GT-BD maps that match as many pairs of observer placed landmarks as possible within distortion bound $K = 1.5$, but without “ground truth” correspondences between observer placed landmarks; (c) continuous Procrustes distance [2]; (d) Procrustes distance induced by GT^2 -BD maps that match as many observed placed landmarks as possible within distortion bound $K = 1.5$, with “ground truth” correspondences between observer placed landmarks as initial matching candidates. Each polygon encloses a collection of individual specimens of closely related species expected to be similar based on visual inspection and traditional comparative analyses. Similar ordination plots for GP_{Euc} or GP_{nw} are omitted in this figure because the ordination shown in those two plots are much worse than any of the plots (a)–(d). According to the PERMANOVA test results in Table 3, pairwise surface registration with GP-BD achieves comparable power of separating taxonomic groups as matching “ground truth” landmarks placed by professional comparative biologists.

7 Discussion and Future Work

This paper discusses a greedy algorithm for automatically selecting representative points on compact manifolds, motivated by the methodology of experimental design with Gaussian process prior in statistics. With a carefully modified heat kernel specified as the covariance function in the Gaussian process prior, our algorithm is capable of producing biologically highly meaningful feature points on some anatomical surfaces. The algorithmically produced landmarks resemble biologists' landmarks selected with expert knowledge, providing adequate coverage for both geometric features and semantically “uncertain” regions on the anatomical surfaces of practical interest. We tested the applicability of this landmarking procedure for various tasks on real datasets.

A future direction of interest is to build theoretical analysis for the optimal experimental design aspects of manifold learning: Whereas existing manifold learning algorithms estimate the underlying manifold from discrete samples, our algorithm concerns economical strategies for encoding geometric information into discrete samples. The landmarking procedure can also be interpreted as a compression scheme for manifolds; correspondingly, the standard manifold learning algorithms may be understood as a decoding mechanism.

The Gaussian process landmarking algorithm presented in this paper takes one anatomical surface as input at one time, which is not exactly consistent with the working style of geometric morphometricians. This special group of biologists are trained to identify semantically meaningful features not only based upon each individual shape in hand but also with respect to the consistency of “global information” presented over the entire shape collection. In the standard practice, landmarking a new anatomical surface typically involve repeated comparisons with all the other surfaces in the collection, and the already placed landmarks on a surface are still subject to change upon future knowledge acquired from landmarking more surfaces. It would be highly interesting to adapt our algorithm to accommodate for this type of group-wise comparison strategies as well.

Though geometric approaches in general lack the ability to recognize Type 1 landmarks, we think that the similarities between Gaussian process landmarks and user selected Type 2 and Type 3 landmarks, over a number of tests presented in this work, call into question whether user-based selection can be justified when “overall shape” is of interest. In particular, we found the ordination plots to be as successful and in some ways superior to the user-based landmarks in reflecting previous ideas about shape affinities. Given this, whether the ground truth of user-based landmarks is “better” or not becomes subjective. While F -ratios were highest in the user-determined sample, we note that it is highly likely that, for any underdetermined landmarks (e.g. the Type 1 landmarks, Type 3 landmarks, or when trying to place Type 2 landmarks on eroded features like blunted cusp tips) biologists will tend to minimize variance within species. In other words, if there is not enough geometry to allow consistent placement of a point, users are likely to unconsciously choose a positioning that visually maximizes similarity to other members of the species (actually, it would be hard to justify doing anything else). Given the likely bias towards minimizing within group error by biologists during landmarking, it is quite remarkable that the Gaussian process approach comes so close to the “ground truth”, and exceeds by so much the other automated methods in terms of F -ratio. In user placed landmarks, there is also the question of how many and which landmarks were chosen, not to mention whether one user has more error in placing the same landmarks than another. Finally, there is the limitation that any traditional landmark used must be present in every specimen of the sample. Given all the issues with the traditional user placed approach, and the demonstrated ability of Gaussian process to emulate qualitatively and quantitatively Type 2 and Type 3 landmarks, we recommend avoiding hand-placement of such landmarks.

Last but not the least, this work stems from an attempt to impose Gaussian process priors on diffeomorphisms between distinct but comparable biological structures, with which a rigorous Bayesian statistical framework for biological surface registration may be developed. The motivation is to measure the uncertainty of pairwise bijective correspondences automatically computed from geometry processing and computer vision techniques. We hope this conditional covariance based landmarking algorithm will shed light upon generalizing covariance structures from a single shape to pairs or even collections of shapes.

A Proof of Theorem 1

Proof of Theorem 1. Recall from [130](or [32, Lemma 8], [131, Lemma B.10]) that

$$\frac{1}{(2\pi\epsilon)^{\frac{d}{2}}} \int_M \exp\left(-\frac{\|x-y\|^2}{2\epsilon}\right) f(y) \, d\text{Vol}(y) = f(x) + \frac{\epsilon}{2} [E(x)f(x) + \Delta f(x)] + O(\epsilon^{\frac{3}{2}}) \quad \text{as } \epsilon \rightarrow 0 \quad (46)$$

where E is a scalar function of the curvature of M at $x \in M$. Thus

$$\exp[-V(z)] \int_M \exp\left(-\frac{\|z-y\|^2}{2\epsilon}\right) f(y) d\text{Vol}(y) = (2\pi\epsilon)^{\frac{d}{2}} \exp[-V(z)] \left\{ f(z) + \frac{\epsilon}{2} [E(z) f(z) + \Delta f(z)] + O\left(\epsilon^{\frac{3}{2}}\right) \right\}. \quad (47)$$

Replacing the function f in (46) with the right hand side of (47), we have

$$\begin{aligned} & \int_M \int_M \exp\left(-\frac{\|x-z\|^2}{2\epsilon}\right) \exp[-V(z)] \exp\left(-\frac{\|z-y\|^2}{2\epsilon}\right) f(y) d\text{Vol}(z) d\text{Vol}(y) \\ &= (2\pi\epsilon)^d \left\{ \exp[-V(x)] \left\{ f(x) + \frac{\epsilon}{2} [E(x) f(x) + \Delta f(x)] + O\left(\epsilon^{\frac{3}{2}}\right) \right\} \right. \\ & \quad \left. + \frac{\epsilon}{2} E(x) \exp[-V(x)] \left\{ f(x) + \frac{\epsilon}{2} [E(x) f(x) + \Delta f(x)] + O\left(\epsilon^{\frac{3}{2}}\right) \right\} \right. \\ & \quad \left. + \frac{\epsilon}{2} \Delta \left(\exp[-V(x)] \left\{ f(x) + \frac{\epsilon}{2} [E(x) f(x) + \Delta f(x)] + O\left(\epsilon^{\frac{3}{2}}\right) \right\} \right) + O\left(\epsilon^{\frac{3}{2}}\right) \right\} \\ &= (2\pi\epsilon)^d \left\{ f(x) \exp[-V(x)] \right. \\ & \quad \left. + \frac{\epsilon}{2} \left\{ [E(x) f(x) + \Delta f(x)] \exp[-V(x)] + f(x) E(x) \exp[-V(x)] + \Delta(f(x) \exp[-V(x)]) \right\} + O\left(\epsilon^{\frac{3}{2}}\right) \right\} \quad \text{as } \epsilon \rightarrow 0. \end{aligned}$$

Plugging the right hand side above into the numerator of the left hand side of (22), and replacing the denominator with the same expression as the numerator except for setting $f \equiv 1$ in (22), we obtain, as $\epsilon \rightarrow 0$,

$$\begin{aligned} & \frac{\int_M \int_M \exp\left(-\frac{\|x-z\|^2}{2\epsilon}\right) \exp[-V(z)] \exp\left(-\frac{\|z-y\|^2}{2\epsilon}\right) f(y) d\text{Vol}(z) d\text{Vol}(y)}{\int_M \int_M \exp\left(-\frac{\|x-z\|^2}{2\epsilon}\right) \exp[-V(z)] \exp\left(-\frac{\|z-y\|^2}{2\epsilon}\right) d\text{Vol}(z) d\text{Vol}(y)} \\ &= \frac{f(x) \exp[-V(x)] + \frac{\epsilon}{2} \left\{ [E(x) f(x) + \Delta f(x)] \exp[-V(x)] + f(x) E(x) \exp[-V(x)] + \Delta(f(x) \exp[-V(x)]) \right\} + O\left(\epsilon^{\frac{3}{2}}\right)}{\exp[-V(x)] + \frac{\epsilon}{2} \left\{ E(x) \exp[-V(x)] + E(x) \exp[-V(x)] + \Delta \exp[-V(x)] \right\} + O\left(\epsilon^{\frac{3}{2}}\right)} \\ &= \left\{ f(x) + \frac{\epsilon}{2} \left[2E(x) f(x) + \Delta f(x) + \exp[V(x)] \Delta(f(x) \exp[-V(x)]) \right] + O\left(\epsilon^{\frac{3}{2}}\right) \right\} \times \\ & \quad \left\{ 1 - \frac{\epsilon}{2} (2E(x) + \exp[V(x)] \Delta \exp[-V(x)]) + O\left(\epsilon^{\frac{3}{2}}\right) \right\} \\ &= f(x) + \frac{\epsilon}{2} \left[2E(x) f(x) + \Delta f(x) + \exp[V(x)] \Delta(f(x) \exp[-V(x)]) - 2E(x) f(x) - f(x) \exp[V(x)] \Delta \exp[-V(x)] \right] + O\left(\epsilon^{\frac{3}{2}}\right) \\ &= f(x) + \frac{\epsilon}{2} [\Delta f(x) + \exp[V(x)] \Delta(f(x) \exp[-V(x)]) - f(x) \exp[V(x)] \Delta \exp[-V(x)]] + O\left(\epsilon^{\frac{3}{2}}\right) \\ &= f(x) + \frac{\epsilon}{2} (2\Delta f(x) - 2\nabla f(x) \cdot \nabla V(x)) + O\left(\epsilon^{\frac{3}{2}}\right) = f(x) + \epsilon (\Delta f(x) - \nabla f(x) \cdot \nabla V(x)) + O\left(\epsilon^{\frac{3}{2}}\right). \end{aligned}$$

This completes the proof. \square

Acknowledgement TG would also like to thank Peng Chen (peng@ices.utexas.edu) at The University of Texas at Austin for pointers to the reduced basis method literature, and Chen-Yun Lin (cylin@math.duke.edu) at Duke University for many useful discussions on heat kernel estimates. The authors would also like to thank Shaobo Han (shaobo.han@duke.edu), Rob Ravier (robert.ravier@duke.edu), and Shan Shan (shan.shan@duke.edu) for inspirational discussions. This work is supported by Simons Math+X Investigators Award #400837 and NSF CAREER Award BCS-1552848.

References

- [1] D. C. ADAMS, F. J. ROHLF, AND D. E. SLICE, *A Field Comes of Age: Geometric Morphometrics in the 21st Century*, *Hystrix*, 24 (2013), pp. 7–14.
- [2] R. AL-AIFARI, I. DAUBECHIES, AND Y. LIPMAN, *Continuous Procrustes Distance Between Two Surfaces*, *Communications on Pure and Applied Mathematics*, 66 (2013), pp. 934–964.
- [3] P. ALLIEZ, D. COHEN-STEINER, O. DEVILLERS, B. LÉVY, AND M. DESBRUN, *Anisotropic Polygonal Remeshing*, *ACM Trans. Graph.*, 22 (2003), pp. 485–493.
- [4] M. J. ANDERSON, *A New Method for Non-Parametric Multivariate Analysis of Variance*, *Austral Ecology*, 26 (2001), pp. 32–46.
- [5] M. ATIYAH AND P. SUTCLIFFE, *The Geometry of Point Particles*, in *Proceedings of the Royal Society of London A: Mathematical, Physical and Engineering Sciences*, vol. 458, The Royal Society, 2002, pp. 1089–1115.
- [6] A. ATKINSON, A. DONEV, AND R. TOBIAS, *Optimum Experimental Designs, with SAS*, vol. 34, Oxford University Press, 2007.
- [7] M. AUBRY, U. SCHLICKEWEI, AND D. CREMERS, *The Wave Kernel Signature: A Quantum Mechanical Approach to Shape Analysis*, in *Computer Vision Workshops (ICCV Workshops), 2011 IEEE International Conference on*, IEEE, 2011, pp. 1626–1633.
- [8] T. F. BANCHOFF, *Critical Points and Curvature for Embedded Polyhedral Surfaces*, *The American Mathematical Monthly*, 77 (1970), pp. 475–485.
- [9] C. BEARD, *Teilhardina. The International Encyclopedia of Primatology. 1–2.*, 2017. DOI: 10.1002/9781119179313.wbprim0444.
- [10] M. BELKIN AND P. NIYOGI, *Laplacian Eigenmaps for Dimensionality Reduction and Data Representation*, *Neural Comput.*, 15 (2003), pp. 1373–1396.
- [11] ———, *Towards a Theoretical Foundation for Laplacian-Based Manifold Methods*, in *Learning Theory*, Springer, 2005, pp. 486–500.
- [12] P. BÉRARD, G. BESSON, AND S. GALLOT, *Embedding Riemannian Manifolds by Their Heat Kernel*, *Geometric & Functional Analysis GAFA*, 4 (1994), pp. 373–398.
- [13] N. BERLINE, E. GETZLER, AND M. VERGNE, *Heat Kernels and Dirac Operators*, Springer, 1992 ed., 12 2003.
- [14] T. BERRY AND J. HARLIM, *Variable Bandwidth Diffusion Kernels*, *Applied and Computational Harmonic Analysis*, 40 (2016), pp. 68–96.
- [15] A. BERTOZZI, X. LUO, A. STUART, AND K. ZYGALAKIS, *Uncertainty Quantification in the Classification of High Dimensional Data*. submitted, 2017.
- [16] P. BINEV, A. COHEN, W. DAHMEN, R. DEVORE, G. PETROVA, AND P. WOJTASZCZYK, *Convergence Rates for Greedy Algorithms in Reduced Basis Methods*, *SIAM journal on mathematical analysis*, 43 (2011), pp. 1457–1472.
- [17] F. L. BOOKSTEIN, *Morphometric Tools for Landmark Data: Geometry and Biology*, Cambridge University Press, 1991.
- [18] D. M. BOYER, L. COSTEUR, AND Y. LIPMAN, *Earliest Record of Platychoerops (Primates, Plesiadapidae), a new species from Mouras Quarry, Mont de Berru, France*, *American Journal of Physical Anthropology*, 149 (2012), pp. 329–346.
- [19] D. M. BOYER, Y. LIPMAN, E. ST. CLAIR, J. PUENTE, B. A. PATEL, T. FUNKHOUSER, J. JERNVALL, AND I. DAUBECHIES, *Algorithms to Automatically Quantify the Geometric Similarity of Anatomical Surfaces*, *Proceedings of the National Academy of Sciences*, 108 (2011), pp. 18221–18226.

[20] D. M. BOYER, J. PUENTE, J. T. GLADMAN, C. GLYNN, S. MUKHERJEE, G. S. YAPUNCICH, AND I. DAUBECHIES, *A New Fully Automated Approach for Aligning and Comparing Shapes*, *The Anatomical Record*, 298 (2015), pp. 249–276.

[21] D. M. BOYER, S. TOUSSAINT, AND M. GODINOT, *Postcranial of the Most Primitive Euprimate and Implications for Primate Origins*, *Journal of Human Evolution*, 111 (2017), pp. 202–215.

[22] A. M. BRONSTEIN, *Spectral Descriptors for Deformable Shapes*, arXiv preprint arXiv:1110.5015, (2011).

[23] A. BUFFA, Y. MADAY, A. T. PATERA, C. PRUD'HOMME, AND G. TURINICI, *A Priori Convergence of the Greedy Algorithm for the Parametrized Reduced Basis Method*, *ESAIM: Mathematical Modelling and Numerical Analysis*, 46 (2012), pp. 595–603.

[24] U. CASTELLANI, M. CRISTANI, S. FANTONI, AND V. MURINO, *Sparse Points Matching by Combining 3D Mesh Saliency with Statistical Descriptors*, *Computer Graphics Forum*, 27 (2008), pp. 643–652.

[25] I. CASTILLO, G. KERKYACHARIAN, AND D. PICARD, *Thomas Bayes' Walk on Manifolds*, *Probability Theory and Related Fields*, 158 (2014), pp. 665–710.

[26] K. N. CHAUDHURY, Y. KHOO, AND A. SINGER, *Global Registration of Multiple Point Clouds using Semidefinite Programming*, *SIAM Journal on Optimization*, 25 (2015), pp. 468–501.

[27] X. CHENG, A. CLONINGER, AND R. R. COIFMAN, *Two-Sample Statistics Based on Anisotropic Kernels*, arXiv preprint arXiv:1709.05006, (2017).

[28] K. CLARKE AND R. GREEN, *Statistical Design and Analysis for a 'Biological Effects' Study*, *Marine Ecology Progress Series*, (1988), pp. 213–226.

[29] K. R. CLARKE, *Non-Parametric Multivariate Analyses of Changes in Community Structure*, *Austral Ecology*, 18 (1993), pp. 117–143.

[30] D. COHEN-STEINER AND J.-M. MORVAN, *Restricted Delaunay Triangulations and Normal Cycle*, in *Proceedings of the nineteenth annual symposium on Computational geometry*, ACM, 2003, pp. 312–321.

[31] D. A. COHN, Z. GHAHRAMANI, AND M. I. JORDAN, *Active Learning with Statistical Models*, *Journal of Artificial Intelligence Research*, 4 (1996), pp. 129–145.

[32] R. R. COIFMAN AND S. LAFON, *Diffusion Maps*, *Applied and Computational Harmonic Analysis*, 21 (2006), pp. 5–30. Special Issue: Diffusion Maps and Wavelets.

[33] N. CRESSIE, *Statistics for Spatial Data*, Wiley Series in Probability and Statistics, John Wiley & Sons, Inc., 2015.

[34] N. CRISTIANINI AND J. SHAWE-TAYLOR, *An Introduction to Support Vector Machines and Other Kernel-Based Learning Methods*, Cambridge University Press Cambridge, 2000.

[35] L. CUEL, J.-O. LACHAUD, Q. MÉRIGOT, AND B. THIBERT, *Robust Geometry Estimation Using the Generalized Voronoi Covariance Measure*, *SIAM Journal on Imaging Sciences*, 8 (2015), pp. 1293–1314.

[36] W. CZAJA AND M. EHLER, *Schroedinger Eigenmaps for the Analysis of Biomedical Data*, *IEEE Transactions on Pattern Analysis and Machine Intelligence*, 35 (2013), pp. 1274–1280.

[37] R. DEVORE, G. PETROVA, AND P. WOJTASZCZYK, *Greedy Algorithms for Reduced Bases in Banach Spaces*, *Constructive Approximation*, 37 (2013), pp. 455–466.

[38] I. L. DRYDEN AND K. V. MARDIA, *Statistical Shape Analysis*, vol. 4, John Wiley & Sons New York, 1998.

[39] T. E. FRICKER, J. E. OAKLEY, AND N. M. URBAN, *Multivariate Gaussian Process Emulators with Nonseparable Covariance Structures*, *Technometrics*, 55 (2013), pp. 47–56.

[40] D. S. FRY, *Shape Recognition Using Metrics on the Space of Shapes*, PhD thesis, Harvard University, Cambridge, MA, USA, 1993. UMI Order No. GAX94-12337.

[41] E. FUSELIER AND G. B. WRIGHT, *Scattered Data Interpolation on Embedded Submanifolds with Restricted Positive Definite Kernels: Sobolev Error Estimates*, SIAM Journal on Numerical Analysis, 50 (2012), pp. 1753–1776.

[42] T. GAO, *Hypoelliptic Diffusion Maps and Their Applications in Automated Geometric Morphometrics*, PhD thesis, Duke University, 2015.

[43] ———, *The Diffusion Geometry of Fibre Bundles*, submitted, (2016). arXiv:1602.02330.

[44] T. GAO, J. BRODZKI, AND S. MUKHERJEE, *The Geometry of Synchronization Problems and Learning Group Actions*, arXiv preprint arXiv:1610.09051, (2016).

[45] T. GAO, G. S. YAPUNCICH, I. DAUBECHIES, S. MUKHERJEE, AND D. M. BOYER, *Development and Assessment of Fully Automated and Globally Transitive Geometric Morphometric Methods, With Application to a Biological Comparative Dataset With High Interspecific Variation*, The Anatomical Record, (2017), pp. n/a–n/a. Submitted.

[46] L. Z. GARAMSZEGI, *Modern Phylogenetic Comparative Methods and Their Application in Evolutionary Biology, Concepts and Practice*. London, UK: Springer, (2014).

[47] J. W. GIDLEY, *Paleocene Primates of the Fort Union, with Discussion of Relationships of Eocene Primates*, Proceedings of the United States National Museum, 63 (1923), pp. 1–38.

[48] P. D. GINGERICH, *Cranial Anatomy and Evolution of Early Tertiary Plesiadapidae (Mammalia, Primates)*, University of Michigan Papers on Paleontology, 15 (1976), pp. 1–141.

[49] ———, *Radiation of Eocene adapidae in Europe*, Geobios, 10 (1977), pp. 165–182.

[50] ———, *Early Eocene *Cantius torresi*—oldest Primate of Modern Aspect from North America*, Nature, 319 (1986), pp. 319–321.

[51] M. GODINOT, *Primate Origins: A Reappraisal of Historical Data Favoring Tupaiid Affinities*, Primate Origins: Adaptations and Evolution. Springer, New York, (2007), pp. 83–142.

[52] T. F. GONZALEZ, *Clustering to Minimize the Maximum Intercluster Distance*, Theoretical Computer Science, 38 (1985), pp. 293–306.

[53] P. I. GOOD, *Permutation, Parametric, and Bootstrap Tests of Hypotheses (Springer Series in Statistics)*, Springer-Verlag New York, Inc., Secaucus, NJ, USA, 2004.

[54] J. C. GOWER, *Generalized Procrustes Analysis*, Psychometrika, 40 (1975), pp. 33–51.

[55] J. C. GOWER AND G. B. DIJKSTERHUIS, *Procrustes Problems*, vol. 3 of Oxford Statistical Science Series, Oxford University Press Oxford, 2004.

[56] A. GRIGOR’YAN, *Heat Kernels on Weighted Manifolds and Applications*, Cont. Math, 398 (2006), pp. 93–191.

[57] V. GUILLEMIN AND A. POLLACK, *Differential Topology*, vol. 370, American Mathematical Soc., 2010.

[58] B. GÜNEYSU, *The Feynman-Kac Formula for Schrödinger Operators on Vector Bundles over Complete Manifolds*, Journal of Geometry and Physics, 60 (2010), pp. 1997–2010.

[59] D. HARDIN AND E. SAFF, *Minimal Riesz Energy Point Configurations for Rectifiable d-Dimensional Manifolds*, Advances in Mathematics, 193 (2005), pp. 174–204.

[60] E. HARJUNMAA, A. KALLONEN, M. VOUTILAINEN, K. HÄMÄLÄINEN, M. L. MIKKOLA, AND J. JERNVALL, *On the Difficulty of Increasing Dental Complexity*, Nature, 483 (2012), pp. 324–327.

[61] E. HARJUNMAA, K. SEIDEL, T. HÄKKINEN, E. RENVOISÉ, I. J. CORFE, A. KALLONEN, Z.-Q. ZHANG, A. R. EVANS, M. L. MIKKOLA, I. SALAZAR-CIUDAD, ET AL., *Replaying Evolutionary Transitions From the Dental Fossil Record*, Nature, 512 (2014), pp. 44–48.

[62] B. R. HASSETT AND T. LEWIS-BALE, *Comparison of 3D Landmark and 3D Dense Cloud Approaches to Hominin Mandible Morphometrics Using Structure-From-Motion*, Archaeometry, 59 (2017), pp. 191–203. ARCH-05-0070-2015.R2.

[63] E. HEBEY, *Nonlinear Analysis on Manifolds: Sobolev Spaces and Inequalities*, vol. 5, American Mathematical Soc., 2000.

[64] B. HELFFER AND J. SJÖSTRAND, *Puits Multiples en Mécanique Semi-Classique iv Etude du Complexe de Witten*, Communications in partial differential equations, 10 (1985), pp. 245–340.

[65] E. HSU, *Estimates of Derivatives of the Heat Kernel on a Compact Riemannian Manifold*, Proceedings of the american mathematical society, 127 (1999), pp. 3739–3744.

[66] A. KAPOOR, K. GRAUMAN, R. URTASUN, AND T. DARRELL, *Active Learning with Gaussian Processes for Object Categorization*, in Computer Vision, 2007. ICCV 2007. IEEE 11th International Conference on, IEEE, 2007, pp. 1–8.

[67] L. KARP AND M. PINSKY, *Volume of a Small Extrinsic Ball in a Submanifold*, Bulletin of the London Mathematical Society, 21 (1989), pp. 87–92.

[68] D. G. KENDALL, *Shape Manifolds, Procrustean Metrics, and Complex Projective Spaces*, Bulletin of the London Mathematical Society, 16 (1984), pp. 81–121.

[69] C.-W. KO, J. LEE, AND M. QUEYRANNE, *An Exact Algorithm for Maximum Entropy Sampling*, Operations Research, 43 (1995), pp. 684–691.

[70] P. KOEHL AND J. HASS, *Landmark-Free Geometric Methods in Biological Shape Analysis*, Journal of The Royal Society Interface, 12 (2015), p. 20150795.

[71] S. Z. KOVALSKY, N. AIGERMAN, R. BASRI, AND Y. LIPMAN, *Large-Scale Bounded Distortion Mappings*, ACM Trans. Graph., 34 (2015), pp. 191–1.

[72] S. Z. KOVALSKY, M. GALUN, AND Y. LIPMAN, *Accelerated quadratic proxy for geometric optimization*, ACM Transactions on Graphics (TOG), 35 (2016), p. 134.

[73] A. KRAUSE, A. SINGH, AND C. GUESTRIN, *Near-Optimal Sensor Placements in Gaussian Processes: Theory, Efficient Algorithms and Empirical Studies*, Journal of Machine Learning Research, 9 (2008), pp. 235–284.

[74] D. D. LEWIS AND W. A. GALE, *A Sequential Algorithm for Training Text Classifiers*, in Proceedings of the 17th annual international ACM SIGIR conference on Research and development in information retrieval, Springer-Verlag New York, Inc., 1994, pp. 3–12.

[75] D. LIANG AND J. PAISLEY, *Landmarking Manifolds with Gaussian Processes.*, in ICML, 2015, pp. 466–474.

[76] L. LIN, M. NIU, P. CHEUNG, AND D. DUNSON, *Extrinsic Gaussian Process (EGPS) for Regression and Classification on Manifolds*. private communication, 2017.

[77] L. LIN, B. ST THOMAS, H. ZHU, AND D. B. DUNSON, *Extrinsic Local Regression on Manifold-Valued Data*, Journal of the American Statistical Association, (2016). to appear.

[78] Y. LIPMAN, *Bounded Distortion Mapping Spaces for Triangular Meshes*, ACM Transactions on Graphics (TOG), 31 (2012), p. 108.

[79] Y. LIPMAN AND I. DAUBECHIES, *Conformal Wasserstein Distances: Comparing Surfaces in Polynomial Time*, Advances in Mathematics, 227 (2011), pp. 1047–1077.

[80] Y. LIPMAN, J. PUENTE, AND I. DAUBECHIES, *Conformal Wasserstein Distance: II. Computational Aspects and Extensions.*, Math. Comput., 82 (2013).

[81] Y. LIPMAN, S. YAGEV, R. PORANNE, D. W. JACOBS, AND R. BASRI, *Feature Matching with Bounded Distortion*, ACM Transactions on Graphics (TOG), 33 (2014), p. 26.

[82] Y.-S. LIU, M. LIU, D. KIHARA, AND K. RAMANI, *Salient Critical Points for Meshes*, in Proceedings of the 2007 ACM symposium on Solid and physical modeling, ACM, 2007, pp. 277–282.

[83] G. G. LORENTZ, M. VON GOLITSCHEK, AND Y. MAKOVZ, *Constructive Approximation: Advanced Problems*, vol. 304, Springer Berlin, 1996.

[84] W. MADYCH AND S. NELSON, *Bounds on Multivariate Polynomials and Exponential Error Estimates for Multi-quadric Interpolation*, Journal of Approximation Theory, 70 (1992), pp. 94–114.

[85] P. MALLIAVIN AND D. W. STROOCK, *Short Time Behavior of the Heat Kernel and Its Logarithmic Derivatives*, Journal of Differential Geometry, 44 (1996), pp. 550–570.

[86] N. MANTEL, *The Detection of Disease Clustering and a Generalized Regression Approach*, Cancer research, 27 (1967), pp. 209–220.

[87] A. MARTINEZ-FINKELSTEIN, V. MAYMESKUL, E. RAKHMANOV, AND E. SAFF, *Asymptotics for Minimal Discrete Riesz Energy on Curves in R^d* , Canad. J. Math, 56 (2004), pp. 529–552.

[88] S. MELZI, E. RODOLÀ, U. CASTELLANI, AND M. M. BRONSTEIN, *Localized Manifold Harmonics for Spectral Shape Analysis*, in Computer Graphics Forum, Wiley Online Library, 2017.

[89] P. MITTEROECKER AND P. GUNZ, *Advances in Geometric Morphometrics*, Evolutionary Biology, 36 (2009), pp. 235–247.

[90] P. MITTEROECKER AND S. M. HUTTEGGER, *The Concept of Morphospaces in Evolutionary and Developmental Biology: Mathematics and Metaphors*, Biological Theory, 4 (2009), pp. 54–67.

[91] C. MOENNING AND N. A. DODGSON, *Fast Marching Farthest Point Sampling*, tech. rep., University of Cambridge, Computer Laboratory, 2003.

[92] M. MOHRI, A. ROSTAMIZADEH, AND A. TALWALKAR, *Foundations of Machine Learning*, MIT press, 2012.

[93] S. MOLNAR, *On the Convergence of the Kriging Method*, in Annales Univ Sci Budapest Sect Comput, vol. 6, 1985, pp. 81–90.

[94] B. NADLER, S. LAFON, R. R. COIFMAN, AND I. G. KEVREKIDIS, *Diffusion Maps, Spectral Clustering and Reaction Coordinates of Dynamical Systems*, Applied and Computational Harmonic Analysis, 21 (2006), pp. 113–127.

[95] A. NAOR, O. REGEV, AND T. VIDICK, *Efficient Rounding for the Noncommutative Grothendieck Inequality*, in Proceedings of the forty-fifth annual ACM symposium on Theory of computing, ACM, 2013, pp. 71–80.

[96] F. J. NARCOWICH, J. D. WARD, AND H. WENDLAND, *Sobolev Error Estimates and a Bernstein Inequality for Scattered Data Interpolation via Radial Basis Functions*, Constructive Approximation, 24 (2006), pp. 175–186.

[97] G. L. NEMHAUSER, L. A. WOLSEY, AND M. L. FISHER, *An Analysis of Approximations for Maximizing Submodular Set Functions-I*, Mathematical Programming, 14 (1978), pp. 265–294.

[98] A. NEMIROVSKI, *Sums of Random Symmetric Matrices and Quadratic Optimization under Orthogonality Constraints*, Mathematical programming, 109 (2007), pp. 283–317.

[99] T. E. NICHOLS AND A. P. HOLMES, *Nonparametric Permutation Tests for Functional Neuroimaging: A Primer with Examples*, Human brain mapping, 15 (2002), pp. 1–25.

[100] S. NIRANJAN, A. KRAUSE, S. M. KAKADE, AND M. SEEGER, *Gaussian Process Optimization in the Bandit Setting: No Regret and Experimental Design*, in Proceedings of the 27th International Conference on Machine Learning, 2010.

[101] J. E. OAKLEY AND A. O'HAGAN, *Probabilistic Sensitivity Analysis of Complex Models: A Bayesian Approach*, Journal of the Royal Statistical Society: Series B (Statistical Methodology), 66 (2004), pp. 751–769.

[102] A. C. ÖZTIRELI, M. ALEXA, AND M. GROSS, *Spectral sampling of manifolds*, ACM Transactions on Graphics (TOG), 29 (2010), p. 168.

- [103] E. PARADIS, *Analysis of Phylogenetics and Evolution with R*, Springer Science & Business Media, 2011.
- [104] F. PESARIN, *Multivariate Permutation Tests: with Applications in Biostatistics*, vol. 240, Wiley Chichester, 2001.
- [105] D. L. PEUTREC, F. NIER, AND C. VITERBO, *Precise Arrhenius Law for p-Forms: The Witten Laplacian and Morse-Barannikov Complex*, Annales Henri Poincaré, 14 (2013), pp. 567–610.
- [106] U. PINKALL AND K. POLTHIER, *Computing Discrete Minimal Surfaces and Their Conjugates*, Experimental mathematics, 2 (1993), pp. 15–36.
- [107] I. PLYUSNIN, A. R. EVANS, A. KARME, A. GIONIS, AND J. JERNVALL, *Automated 3D Phenotype Analysis Using Data Mining*, PLoS One, 3 (2008), p. e1742.
- [108] K. POLTHIER, *Computational Aspects of Discrete Minimal Surfaces*, Proc. of the Clay Summer School on Global Theory of Minimal Surfaces, to appear, (2002).
- [109] J. PUENTE, *Distances and Algorithms to Compare Sets of Shapes for Automated Biological Morphometrics*, PhD thesis, Princeton University, 2013.
- [110] F. PUKELSHEIM, *Optimal Design of Experiments*, SIAM, 2006.
- [111] J. RAMSAY AND B. SILVERMAN, *Functional Data Analysis*, Springer Series in Statistics, Springer, 2005.
- [112] J. O. RAMSAY AND B. W. SILVERMAN, *Applied Functional Data Analysis: Methods and Case Studies*, vol. 77, Springer New York, 2002.
- [113] C. E. RASMUSSEN AND C. K. I. WILLIAMS, *Gaussian Processes for Machine Learning*, Adaptive Computation and Machine Learning, The MIT Press, 2006.
- [114] K. RITTER, *Average-Case Analysis of Numerical Problems*, Springer, 2007.
- [115] F. J. ROHLF AND F. L. BOOKSTEIN, *Proceedings of the Michigan Morphometrics Workshop*, University of Michigan Museum of Zoology, 1990.
- [116] S. ROSENBERG, *The Laplacian on a Riemannian Manifold: An Introduction to Analysis on Manifolds*, no. 31 in London Mathematical Society Student Texts, Cambridge University Press, 1997.
- [117] V. L. ROTH, *On Three-Dimensional Morphometrics, and on the Identification of Landmark Points*, in Contributions to Morphometrics, L. F. Marcus, E. Bello, and G.-V. A., eds., Museo Nacional de Ciencias Naturales, Madrid, 1993, pp. 41–61.
- [118] D. E. RUSSELL, P. LOUIS, AND D. E. SAVAGE, *Primates of the French Early Eocene*, University of California Publications in the Geological Sciences, 73 (1967), pp. 1–46.
- [119] R. B. RUSU AND S. COUSINS, *3D is Here: Point Cloud Library (PCL)*, in IEEE International Conference on Robotics and Automation (ICRA), Shanghai, China, May 9-13 2011.
- [120] J. SACKS, S. B. SCHILLER, AND W. J. WELCH, *Designs for Computer Experiments*, Technometrics, 31 (1989), pp. 41–47.
- [121] A. SALTELLI AND S. TARANTOLA, *On the Relative Importance of Input Factors in Mathematical Models: Safety Assessment for Nuclear Waste Disposal*, Journal of the American Statistical Association, 97 (2002), pp. 702–709.
- [122] T. J. SANTNER, B. J. WILLIAMS, AND W. I. NOTZ, *The Design and Analysis of Computer Experiments*, Springer Series in Statistics, Springer Science & Business Media, 2013.
- [123] B. SCHOLKOPF AND A. J. SMOLA, *Learning with Kernels: Support Vector Machines, Regularization, Optimization, and Beyond*, MIT press, 2001.

[124] J. H. SCHWARTZ AND I. TATTERSALL, *Evolutionary Relationships of Living Lemurs and Lorises (Mammalia, Primates) and Their Potential Affinities with European Eocene Adapidae.*, Anthropological papers of the AMNH; v. 60, pt. 1, (1985).

[125] E. R. SEIFFERT, L. COSTEUR, AND D. M. BOYER, *Tarsal Morphology of Caenopithecus, a Large Adapiform Primate from the Middle Eocene of Switzerland*, PeerJ, 3 (2015), p. e1036.

[126] B. SETTLES, *Active Learning Literature Survey*, University of Wisconsin, Madison, 52 (2010), p. 11.

[127] S.-J. SHEU, *Some Estimates of the Transition Density of a Nondegenerate Diffusion Markov Process*, The Annals of Probability, (1991), pp. 538–561.

[128] M. T. SILCOX, *Plesiadapiform. The International Encyclopedia of Primatology. 1–2.*, 2017. DOI: 10.1002/9781119179313.wbprim0038.

[129] E. L. SIMONS, *A New Eocene Primate Genus, Cantius, and a Revision of Some Allied European Lemuroids*, vol. 7, British Museum, 1962.

[130] A. SINGER, *From Graph to Manifold Laplacian: The Convergence Rate*, Applied and Computational Harmonic Analysis, 21 (2006), pp. 128–134.

[131] A. SINGER AND H.-T. WU, *Vector Diffusion Maps and the Connection Laplacian*, Communications on Pure and Applied Mathematics, 65 (2012), pp. 1067–1144.

[132] J. SMITH AND S. SCHAEFER, *Bijective parameterization with free boundaries*, ACM Transactions on Graphics (TOG), 34 (2015), p. 70.

[133] K. SMITH, *On the Standard Deviations of Adjusted and Interpolated Values of an Observed Polynomial Function and its Constants and the Guidance They Give Towards a Proper Choice of the Distribution of Observations*, Biometrika, 12 (1918), pp. 1–85.

[134] O. SMOLYANOV, H. WEIZSÄCKER, AND O. WITTICH, *Brownian Motion on a Manifold as Limit of Stepwise Conditioned Standard Brownian Motions*, Stochastic Processes, Physics and Geometry: New Interplays, II, 29 (2000), pp. 589–602.

[135] O. G. SMOLYANOV, H. v WEIZSÄCKER, AND O. WITTICH, *Chernoff's Theorem and Discrete Time Approximations of Brownian Motion on Manifolds*, Potential Analysis, 26 (2007), pp. 1–29.

[136] A. M.-C. SO, *Moment Inequalities for Sums of Random Matrices and Their Applications in Optimization*, Mathematical Programming, 130 (2011), pp. 125–151.

[137] M. L. STEIN, *Interpolation of Spatial Data: Some Theory for Kriging*, Springer Science & Business Media, 2012.

[138] D. W. STROOCK AND J. TURETSKY, *Upper Bounds on Derivatives of the Logarithm of the Heat Kernel*, Communications in Analysis and Geometry, 6 (1998), pp. 669–685.

[139] G. K. TAM, Z.-Q. CHENG, Y.-K. LAI, F. C. LANGBEIN, Y. LIU, D. MARSHALL, R. R. MARTIN, X.-F. SUN, AND P. L. ROSIN, *Registration of 3D Point Clouds and Meshes: A Survey from Rigid to Nonrigid*, IEEE Transactions on Visualization and Computer Graphics, 19 (2013), pp. 1199–1217.

[140] A. B. TSYBAKOV, *Introduction to Nonparametric Estimation*, Springer Publishing Company, Incorporated, 1st ed., 2008.

[141] K. TURNER, S. MUKHERJEE, AND D. M. BOYER, *Persistent homology transform for modeling shapes and surfaces*, Information and Inference: A Journal of the IMA, 3 (2014), pp. 310–344.

[142] A. W. VAN DER VAART AND J. H. VAN ZANTEN, *Reproducing Kernel Hilbert Spaces of Gaussian Priors*, in Pushing the Limits of Contemporary Statistics: Contributions in Honor of Jayanta K. Ghosh, Institute of Mathematical Statistics, 2008, pp. 200–222.

[143] N. VITEK, C. MANZ, T. GAO, J. BLOCH, S. STRAIT, AND D. M. BOYER, *Semi-supervised Determination of Pseudocryptic Morphotypes Using Observer-free Characterizations of Anatomical Alignment and Shape*. Accepted, 2017.

[144] W. WANG, R. TUO, AND C. J. WU, *Universal Convergence of Kriging*, arXiv preprint arXiv:1710.06959, (2017).

[145] H. WENDLAND, *Scattered Data Approximation*, vol. 17, Cambridge University Press, 2004.

[146] H.-T. WU, *Embedding Riemannian Manifolds by the Heat Kernel of the Connection Laplacian*, Advances in Mathematics, 304 (2017), pp. 1055–1079.

[147] Z.-M. WU AND R. SCHABACK, *Local Error Estimates for Radial Basis Function Interpolation of Scattered Data*, IMA Journal of Numerical Analysis, 13 (1993), pp. 13–27.

[148] Y. YANG AND D. B. DUNSON, *Bayesian Manifold Regression*, The Annals of Statistics, 44 (2016), pp. 876–905.

[149] G. S. YAPUNCICH, E. R. SEIFFERT, AND D. M. BOYER, *Quantification of the Position and Depth of the Flexor Hallucis Longus Groove in Euarchontans, with Implications for the Evolution of Primate Positional Behavior*, American Journal of Physical Anthropology, 163 (2017), pp. 367–406.

[150] D. YLVISAKER, *Designs on Random Fields*, A Survey of Statistical Design and Linear Models, 37 (1975), pp. 593–607.

[151] M. L. ZELDITCH, D. L. SWIDERSKI, AND H. D. SHEETS, eds., *Geometric Morphometrics for Biologists: A Primer*, Academic Press, San Diego, second ed., 2012.